Experiments in Fluids (2025) 66:26
https://doi.org/10.1007/s00348-024-03945-3

RESEARCH ARTICLE

The effects of wall proximity on the turbulent flow field in a square duct structured with detached divergent ribs on one wall

Sebastian Ruck[1] · **Isaac Lorenzo Mercado**[1]

Received: 25 August 2024 / Revised: 2 December 2024 / Accepted: 14 December 2024 / Published online: 21 January 2025

Abstract

The effect of the wall proximity of detached 60° divergent ribs applied on one wall in a square duct on the turbulent flow field was investigated. Laser Doppler anemometry (LDA) measurements were conducted for different clearance-to-rib-height ratios in the range of 0.1–1.0 at a Reynolds number (based on the rib height and mean bulk velocity) of 5000. Mean velocities, Reynolds stresses, triple velocity correlations as well as skewness and kurtosis were determined and yield deep insights into the turbulent flow field. The results showed that a geometry-induced secondary fluid motion occurred above and below the rib. The variations in the highly three-dimensional flow field close to the ribs and the geometry-induced secondary flow motion with the clearance-to-rib-height ratio determined the development of the wall-bounded flows and separating shear layers. Large recirculation regions on the bottom duct wall were prevented by the fluid exiting the gap below the detached ribs and separated shear layers pivoted upward in lateral direction. With decreasing wall proximity, lower mean vertical flow velocities above the ribs and the increasing upward fluid flow originating from the flow in the gap attenuated an intense interaction of the separated shear layers with the wall-bounded flow within the inter-rib spacing. Since turbulent structures originated in the shear layers, distributions of high-order statistic moments depend strongly on the shear layer development. Reynolds stresses and triple velocity correlations increased in the direction of the side walls near the rib due to the lateral flow motion, and their peak regions moved away from the wall with increasing clearance-to-rib-height ratios.

1 Introduction

Turbulent flow physics in rib-roughened ducts are of crucial significance for heat engineering, e.g., internal cooling ducts of solar receivers, gas-cooled nuclear fusion reactor components or turbine blades (Han 2004; Ruck et al. 2019; Bhushan and Singh 2010; Tanda 2011) and have been the subject of intensive research for decades. The turbulent flow field in rectangular ducts roughened by attached(=wall-mounted) ribs is highly complex and affected by several geometrical parameters such as rib-pitch(p)-to-rib-height(k_r) ratio (Liou et al. 1992; Rau et al. 1998), rib-height-to-duct-height(h) ratio (Graham et al. 2004; Jia et al. 2005; Mahmoodi-Jezeh and Wang 2020), rib configuration (Gao and Sundén 2004a, b; Tachie and Shah 2008; Fang et al. 2015; Ruck and Arbeiter 2018) or rib cross-sectional shape (Ahn et al. 2005; Wang and Sundén 2007b; Sreekesh et al. 2021). The development of secondary flow and its interaction with the wall-bounded shear flow at the duct side walls and with the near-rib flow play a major role in the development of the turbulent flow field (Hirota et al. 1992; Mahmoodi-Jezeh and Wang 2020). While transversely oriented ribs cause secondary flows in rectangular ducts due to the high pressure gradient along the ribs and the asymmetry of the flow configuration (Lohász et al. 2006), ribs with elements inclined to the main flow direction provide a production source for the streamwise vorticity (Fang et al. 2015) and, thus, cause strong geometry-induced secondary fluid motion (Olsson and Sundén 1998; Gao and Sundén 2004b; Satta et al. 2012).

In the last decade turbulent flow in square ducts rib-roughened by attached divergent ribs (also called 'V-shaped ribs' in the literature) at one duct wall was investigated in great detail (for a rib-pitch-to-rib-height ratio of $p/k_r = 8.0$, and rib angle of attack in the range from 30° to 60° at a Reynolds number (based on the duct height and mean bulk velocity) of $7.0 \times 10^3 \leq \mathrm{Re}_h \leq 1.3 \times 10^4$) by Fang et al.

✉ Sebastian Ruck
sebastian.ruck@kit.edu

Isaac Lorenzo Mercado
isaac.mercado@kit.edu

[1] Institute of Neutron Physics and Reactor Technology, Karlsruhe Institute of Technology, Hermann-von-Helmholtz-Platz 1, 76344 Eggenstein-Leopoldshafen, Baden-Wuerttemberg, Germany

(2015, 2017) and Mahmoodi-Jezeh and Wang (2022). Here, it was shown that for attached divergent ribs applied on one duct wall strong, secondary flow appears as a pair of large-scale counter-rotating vortices in a streamwise-normal plane. Fluid moves upward above the ribs in the region close to the duct side walls and downward around the duct symmetry plane. Regions of negative mean vertical flow velocity coincide with regions of high positive mean axial velocity above the rib and maxima of positive mean vertical velocity occur near the duct side walls (Fang et al. 2015). Due to the intense lateral and upward fluid motion by secondary flow, highly energetic turbulent vortex structures cluster near the downstream rib end at the smooth duct side walls. The downward fluid motion above the ribs and around the duct symmetry plane displaces the shear layer detaching from the rib crest into the inter-rib spacing and causes an accumulation of high-energy turbulent flow structures in the leeward rib region. Both the high-energy turbulent flow structures above the rib and within the inter-rib spacing appear without a streamwise-elongation in compact form indicating locally quasi-isotropic turbulence. Their population is consistent with the occurrence of peak values of Reynolds normal stresses and turbulence kinetic energy above the rib at the windward and leeward rib region near the duct side walls and within the inter-rib spacing (Fang et al. 2017). Above the rib in the channel central region, turbulence production is weak and significant changes in the distributions in axial direction are lacking. The intense three-dimensional secondary flow above the rib-induced shear layer suppresses the primary mean shear rate in the main flow direction ($\partial\langle u\rangle/\partial y$, $\langle u\rangle$ time-averaged velocity in the main flow direction, y vertical coordinate). In addition, the absence of an interaction between near-rib flow and duct core flow by sweep and ejection events observed for transversely oriented ribs (Cardwell et al. 2011; Wang et al. 2010) results in very low Reynolds shear stresses (Mahmoodi-Jezeh and Wang 2022). Below the shear layer and between the leeward rib surface and the shear layer reattachment point, a recirculation region develops in the wake parallel to the rib from the rib tip to the duct side walls. The position of the mean reattachment point in the inter-rib spacing as well as the size of the recirculation region vary with the angle of attack (Fang et al. 2017). After reattachment of the free shear layer, an attached shear layer develops. The Reynolds stresses decrease further downstream while spatial and temporal length scales of turbulent flow structures decay due to the breakdown of vortical streaks caused by an interaction with the strong secondary flow (Mahmoodi-Jezeh and Wang 2022).

By detaching a rib from the wall by a small clearance c, a gap flow develops below the rib generating a wall-bounded jet at the gap exit. As shown for transversely oriented circular and square cylinders in single or in array configuration (Marumo et al. 1985; Yao et al. 1989; Nakagawa et al. 1998, 1999b; Liou et al. 1995; Ahn and Lee 2010; He et al. 2016), shear layers separating at the upper and lower rib trailing edges interact with the wall-bounded jet flow leading to fundamentally different turbulent flow fields for attached and detached ribs. The occurrence of flow stagnation points and recirculation zones within the inter-rib spacing due to a permanent reattachment of the shear layer separated at the upper rib trailing edge as well as the interaction of vortex structures shed from the rib with the wall-bounded shear flow depend on the clearance-to-rib-height ratio c/k_r (Durão et al. 1991; Bosch et al. 1996; Bailey et al. 2002; Martinuzzi et al. 2003; Wang and Tan 2008). Considering the flow configurations known for transversely oriented detached ribs with different c/k_r and for attached divergent ribs, distinctly different turbulent flow fields strongly affected by geometry-induced secondary fluid motion are expected to occur for detached divergent ribs at varying c/k_r. However, systematic investigations as well as detailed studies about the effect of the rib configuration of detached ribs in rectangular ducts on the turbulent flow physics are lacking so far. This study investigates the effect of the wall proximity of 60° divergent ribs applied on one wall in a square duct on the development of the mean flow field, the rib-induced turbulent transport, and the rib-induced secondary flow field. LDA measurements were performed at a Reynolds number of $\mathrm{Re}_{k_r} = u_B \cdot k_r/\nu = 5000$ (with the bulk flow velocity u_B and the kinematic viscosity ν) and varying clearance-to-rib-height ratios in the range from $c/k_r = 0.1$ to 1.0.

2 Experimental Facility and Methodology

2.1 Test section

Experiments to study turbulent flow in a square duct roughened by detached divergent ribs were carried out in a closed gas loop. The air flow was circulated by two side channel blowers connected in series. Water-cooled heat exchangers were installed downstream of the side channel blowers to compensate the temperature increase by air compression. To reduce velocity and pressure fluctuations as well as swirl effects due to pipe bends in the piping system, a settling tank was located upstream of the entrance duct and the test section, as sketched in Fig. 1 a. The height H and width W of the smooth entrance duct and the rib-roughened test section were 100 mm and 100 mm, respectively. Two 50 mm thick honeycomb meshes with a honeycomb diameter of 6.4 mm (wall thickness 25 µm, porosity $\Phi = 98.6\,\%$) were arranged in series at the beginning of the 2470 mm long entrance duct to minimize large-scale flow inhomogeneities and disturbances due to pipe bends and upstream components. The length of the test section was 2190 mm.

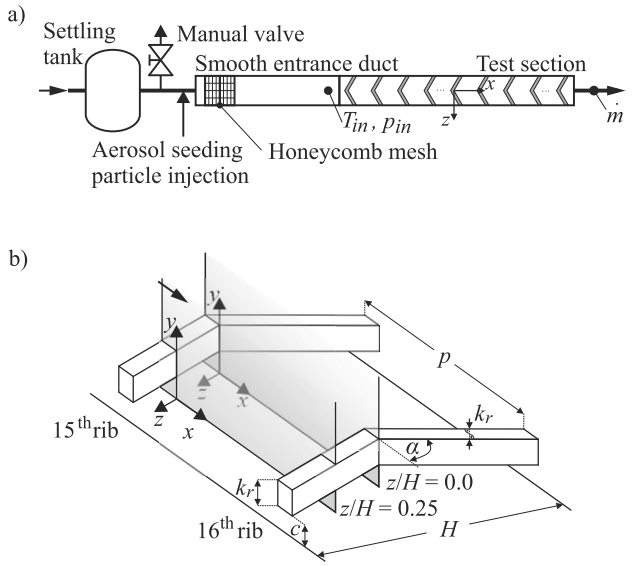

Fig. 1 Experimental setup: **a** Piping diagram of the air loop test facility and **b** sketch of the test section, nomenclature of the rib configuration. The origin of the Cartesian coordinate system (x, y, z) refers to the respective measurement plane ($z/H = 0.0$; $z/H = 0.25$) and is located in the corresponding measuring plane at the rear side of the divergent rib and the duct bottom wall

The bottom duct wall (measured mean surface roughness $Ra = 0.8\,\mu m$) was made of black polyamide, while the side and top duct walls were made of 12.0 mm thick transparent acrylic. All duct walls were mounted in an aluminum frame. As depicted in Fig. 1b, divergent ribs oriented transversely to the axial flow direction with an angle of attack of $\alpha = 60°$ were installed above the bottom duct wall by mounting the ribs into the side walls. The rib cross-sectional shape perpendicular to the lateral rib chord line was squared with $k_r \times k_r$. For each investigated clearance-to-rib-height ratio c/k_r, the divergent ribs were mounted to the corresponding duct side walls. The rib height was $k_r = 10.0$ mm and the rib length was $l_r = 11.5$ mm. The rib pitch was $p = 90.0$ mm, since several studies reported a pitch-to-rib-height ratio in the range of $9 \leq p/k_r \leq 10$ for high heat transfer capability (Rau et al. 1998; Han 1984). The clearance between the ribs and the bottom duct wall was $c = 1.0$ mm, 3.0 mm, 5.0 mm, and 10.0 mm, respectively, leading to a clearance-to-rib-height ratio of $c/k_r = 0.1$, 0.3, 0.5, and 1.0, respectively. The rib edges pointing upstream and downstream are referred to as the rib leading edge and rib trailing edge, respectively. It is noted that the height, width and pitch of the divergent 'ribs' in the present study are much larger than those of 'riblets' which are several viscous units in height, commonly closely spaced and applied in turbulent boundary layer flows for the purpose of skin-friction drag reduction (García-Mayoral and Jiménez 2011; Endrikat et al. 2022).

2.2 Instrumentation

The flow field near rib-roughened surfaces was expected to be three-dimensional and highly unsteady. It is characterized by flow separation at the rib leading edges, flow reattachment on the upper and lower rib surfaces, shear layer separation at the trailing edges, recirculation, and shedding-induced unsteady wake flow. To prevent disturbances of the turbulent flow field by measurement equipment and to resolve the flow field within the narrow gap in detail, non-invasive LDA flow velocity measurements were carried out. The streamwise (x) flow velocity u and the vertical (y) flow velocity v were measured by a Dantec Dynamics Fiber Flow LDA system operating in the backscatter mode with a Burst Spectrum Analyzer Flowmaster P80 for signal processing.

The light provided by a 320 mW Spectra-Physics Ar-Ion laser was transferred to a transmitter unit, where a frequency shift was induced by a Bragg cell and the light was separated by a color splitter into two laser beam pairs with wave lengths of 488.0 nm and 514.5 nm. A 60 mm 2D optical probe with a focal length of $f = 160$ mm was connected by optical cables to the transmitter unit. The probe was mounted sideways to the test section on a three-dimensional ISEL traverse system with spatial resolution of $\pm 10\,\mu m$ in all directions. The axis of the probe was aligned parallel to the lateral axis z (normal to the main flow direction and normal to the vertical direction), resulting in an orientation of the laser beam pairs with a wavelength of 514.5 nm parallel to the $x - z$ plane and in an orientation of laser beam pairs with a wavelength of 488 nm parallel to the $y - z$ plane. The diameters and lengths of the ellipsoidal measurement volumes were 78 µm and 658 µm for 514.5 nm and 74 µm and 625 µm for 488 nm, respectively. Therefore, the measurement point closest to the bottom wall where burst signals could be recorded by the laser beam pairs parallel to the $x - z$ plane was assumed to have a wall distance of $y/k_r = 0.008$. For light scattering, the flow was seeded by aerosol particles with a particle size smaller than $\varnothing \leq 1.0\,\mu m$ (Topas GmbH 2019). These particles were generated from di-ethyl-hexyl-sebacate fluid by a Topas ATM 210/H aerosol generator. The aerosol was injected immediately before the smooth entrance duct. By means of a manual outlet valve, the pressure increase due to the aerosol injection was controlled to ensure a constant mass flow rate in the loop. Since the aerosol particles contaminated the transparent acrylic windows and reduced the data rate and the detected burst quality, the test section was cleaned regularly during a test series.

LDA measurements were carried out for a Reynolds number of $\mathrm{Re}_H = \dot{m} \cdot H^{-1} \cdot \mu(T_{\mathrm{in}})^{-1} = 5.0 \cdot 10^4$, which was determined from the mass flow rate $\dot{m}$ measured by an Endress & Hauser 80/F80 Coriolis flow meter and from the dynamic viscosity of air μ which was approximated by a fourth-order polynomial (VDI 2010) using the inlet fluid

temperature T_{in} measured by an Omega PT100 temperature probe immediately upstream of the test section. The data rate varied with wall distance from less than 100 samples s^{-1} in the immediate vicinity of the wall to 1500 samples s^{-1} in the mid-duct region. Higher data rates were avoided due to statistical error reduction (George 1988). In the present study, 200 000 random samples were recorded at each measurement point, leading to a sufficiently large number of statistically independent samples for minimizing the statistical uncertainties, except for the region close to the side walls where only 50 000 random samples were obtained due to the low data rate. The measurement time per measurement point varied from 130 sec to 2000 sec. Due to the divergent ribs, the wake region behind the rib was inaccessible for the laser beams. The measurement setup and the focal length of the 2D LDA probe enabled measurements of vertical velocity above a certain vertical distance to the wall and rib only. They depended on the clearance-to-rib-height ratio and the measurement plane. The region close to the duct top wall could not be captured due to the experimental setup. The LDA measuring process, including the traverse positioning, was controlled by means of the BSA Flow Software 6.5. At each measurement point, the inlet pressure p_{in}, inlet temperature T_{in}, and mass flow rate $\dot{m}$ were recorded with a measurement frequency of 1 kHz, mean-averaged over 1 sec, and taken into account for the analysis.

2.2.1 Uncertainty

The stochastic uncertainty and the uncertainties originating from the experimental setup and the measurement method make up the measurement uncertainty of the time-averaged quantities. In general, the stochastic uncertainty was determined on the basis of the 95% confidence interval $1.96 \cdot \sqrt{var\{q\}/N}$, with the variance $var\{q\}$ of the measured quantity q and the number of samples N. For the statistical moments of the flow velocities measured point by point, the stochastic uncertainty was calculated for each individual measurement point. Here, the variances were determined by the estimators for arbitrarily distributed samples (Benedict and Gould 1996). To reduce the statistical velocity biasing of the LDA measurements, residence time weighting (Buchhave et al. 1979) was applied for the averaging process. The samples N were given by $t/(2 \cdot T_u)$ (Tennekes and Lumley 1972), with the acquisition time per measurement point t and the integral time scale T_u determined by integrating the autocovariance function of the streamwise velocity up to the first zero crossing.

The uncertainty of ±0.9% for the LDA measurement comprised the uncertainties due to positioning and orientation of the measurement volume, uncertainties due to the flow tracking capability of the tracer particles (for a mean tracer particle diameter of $\varnothing = 0.2\,\mu\text{m}$), and an estimated relative uncertainty of ±0.3% which is typical of commercial LDA measurement systems. The individual uncertainties of the statistical moments of flow velocity at each measurement point are given in bar form in the figures.

For the Reynolds number, the stochastic uncertainty was calculated by assuming normally distributed samples and the number of samples $N = t \cdot 1\text{Hz}$ per measurement point. The mean uncertainty of the Reynolds number averaged over all samples was ±57.

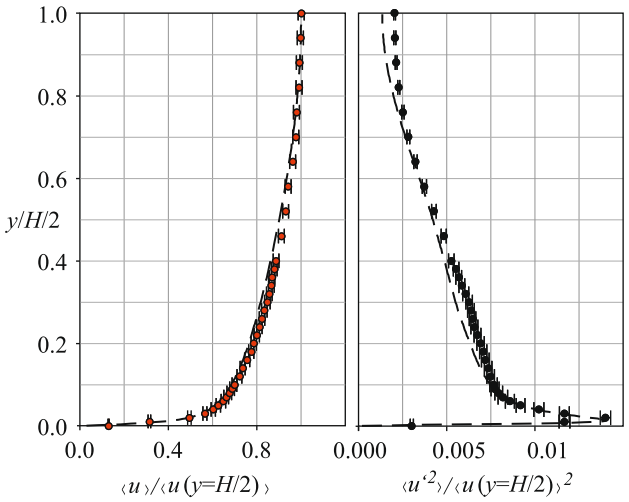

Fig. 2 Characterization of the incoming flow. Normalized • mean streamwise velocity and • streamwise Reynolds normal stress measured at the $z/H = 0.0$-plane of the smooth test section for $\text{Re}_H = 5.0 \cdot 10^4$ ($\text{Re}_\tau = c_f^{0.5} \cdot 2^{-0.5} \cdot u_B \cdot h \cdot \nu(T_{\text{in}})^{-1} \approx 1270$, with the kinematic viscosity for air (VDI 2010) and the friction factor c_f determined from the Filonenko correlation (Petukhov 1970) for smooth ducts) compared with −− DNS results from Pirozzoli et al. (2018) for a turbulent flow in a square duct at the $z/H = 0.0$-plane at $\text{Re}_\tau = 1000$

2.3 Inflow condition and measuring zone

All measurements were taken under nearly steady state conditions. Due to the gradually regulated water-cooled heat exchanger, the time-averaged air temperature T_{in} measured upstream of the test section varied slowly by a maximum of $\Delta T < \pm 0.6\,\text{K}$ during a test series. The averaged inflow turbulence intensity $I = \sqrt{1/2 \cdot (\langle u'^2\rangle + \langle v'^2\rangle)}/\sqrt{(\langle u\rangle^2 + \langle v\rangle^2)}$ in the center at the end of the smooth entrance duct was 4.2%. The normalized mean streamwise velocity $\langle u\rangle/u(y = H/2)$ and the normalized streamwise Reynolds normal stress $\langle u'^2\rangle/u_B^2$ of the turbulent inlet flow over the wall distance are shown in Fig. 2. (In the present study, the time-averaged mean velocities in streamwise and vertical directions are denoted by $\langle u\rangle$ and $\langle v\rangle$, and the corresponding fluctuations of the instantaneous quantities around their time-averaged means are indicated by u' and v', respectively.)

As shown in previous studies of turbulent flow in ducts with attached (Sew and Tafti 2004; Ruck and Arbeiter 2021)

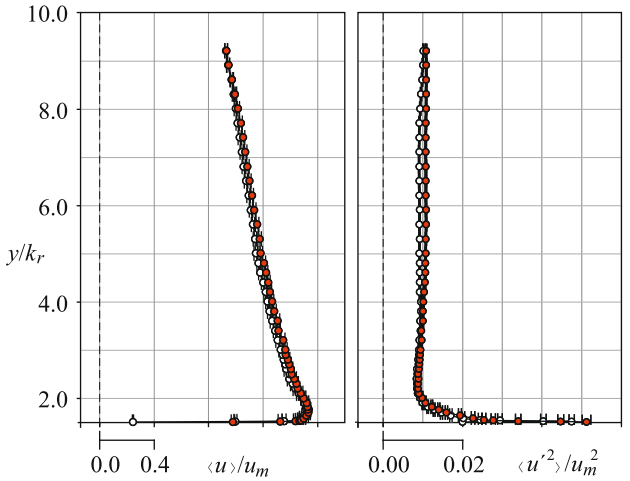

Fig. 3 Normalized mean velocity $\langle u \rangle / u_B$ and normalized axial Reynolds normal stress $\langle u'^2 \rangle / u_B^2$ measured above the 16th rib ∘ $x/k_r = -0.58$ and above the 17th rib • $x/k_r = 8.42$ in the $z/H = 0.0$-plane for $c/k_r = 0.5$

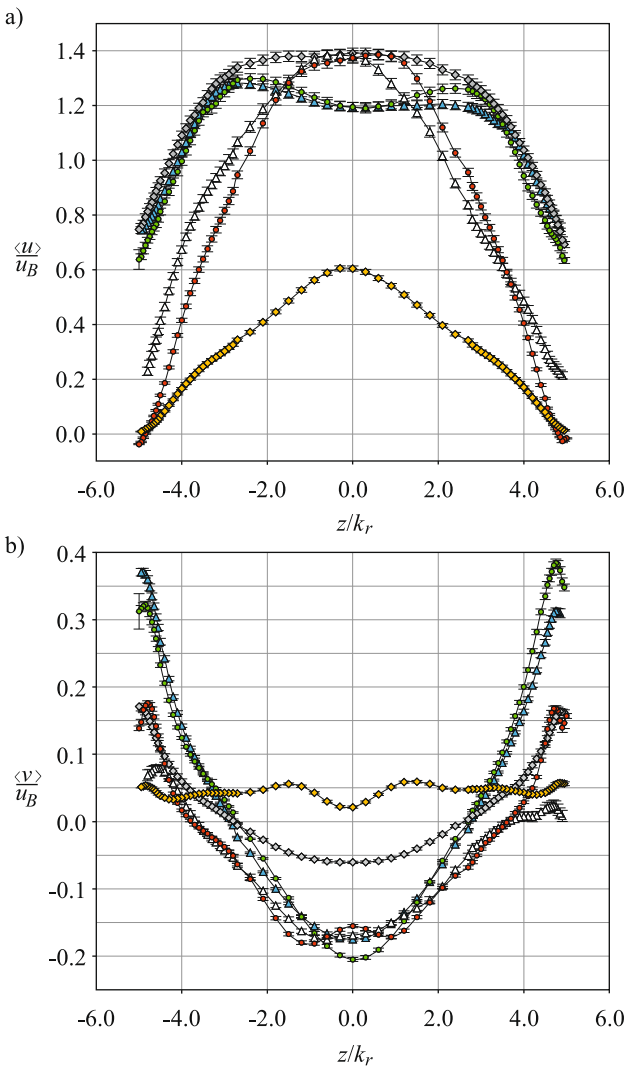

Fig. 4 Normalized **a** axial mean velocity $\langle u \rangle / u_B$ and **b** vertical mean velocity $\langle v \rangle / u_B$ measured along lines parallel to the z-axis at $x/k_r = 4.0$, $y/k_r = 1.3$ for △ $c/k = 0.1$, • 0.3 and ♦ 1.0 and at $x/k_r = 4.0$, $y/k_r = 5.0$ for ▲ $c/k_r = 0.1$, ● 0.3 and ◆ 1.0

or detached transversely oriented square ribs (Liou et al. 1997) having comparable rib parameters k/H and p/k and within similar Reynolds number ranges ($2.0 \cdot 10^4 \leq \mathrm{Re}_H \leq 1.0 \cdot 10^5$ with a Reynolds number based on the duct height and mean bulk velocity), fully developed statistical flow quantities and flow field periodicity between the successive rib-pitch sections can be expected after a developing length of $x/H \geq 12$. Therefore, the measurement region was between the 15th and 16th ribs with a developing length of $\Delta x/H = 12.6$. Confirmation of fully developed flow quantities and flow field periodicity for the measurement region is important to exclude effects of inlet and outlet boundary conditions on the measurement region and to ensure statistical reproducibility of the measurement results. For the verification, the mean velocities and the corresponding higher-order statistical moments were determined and compared in two successive measuring ranges at positions axially offset from each other by a rib spacing p. The distributions of the normalized mean streamwise velocity $\langle u \rangle / u_B$ and the normalized streamwise Reynolds normal stress $\langle u'^2 \rangle / u_B^2$ measured above the 16th rib ($x/k_r = -0.58$) and above the 17th rib ($x/k_r = 8.42$) in the $z/H = 0.0$-plane for $c/k = 0.5$ are shown in Fig. 3. The bulk velocity u_B corresponds to the velocity averaged over cross section and over acquisition time of a measurement series per measurement point. The distributions of mean velocity and Reynolds stress in Fig. 3 are qualitatively and quantitatively similar. The mean deviations between the distributions measured above the 16th rib ($x/k_r = -0.58$) and above the 17th rib ($x/k_r = 8.42$) are $< 2\%$ for $\langle u \rangle / u_B$ and $< 8\%$ for $\langle u'^2 \rangle / u_B^2$, respectively. Due to the minor deviations of the distributions of statistical moments, a quasi-spatial periodicity was assumed in the measurement region between the 15th and 16th ribs. For an entirely spatial periodicity of the turbulent flow field, larger entrance lengths are recommended for divergent detached ribs in square ducts.

To exclude lateral distortion of the flow field, the symmetry of the flow field relative to the $z/H = 0.0$-plane(=duct symmetry plane) in the measuring zone was evaluated by velocity measurements along the z-axis at $x/k_r = 4.0$, $y/k = 1.3$ and $x/k_r = 4.0$, $y/k_r = 5.0$ for $c/k_r = 0.1, 0.3$, and 1.0. With the exception of the area near the side walls at $z/k_r > 4.5$ and $z/k_r < -4.5$, the mean flow field represented by the mean streamwise velocity and mean vertical velocity in Fig. 4 is approximately symmetrical to the duct symmetry plane. The moderate asymmetry near the side walls may be explained by a slightly differently developing flow due to the surface transitions at the duct side walls between the acrylic

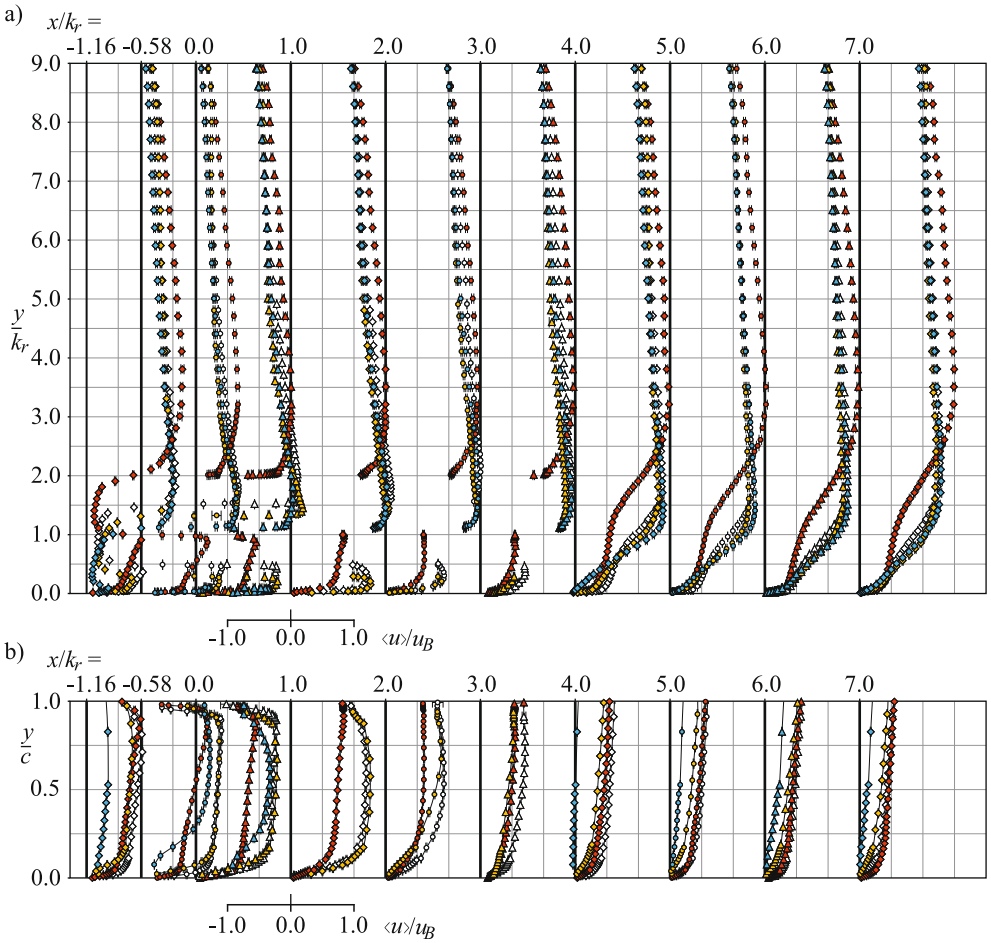

Fig. 5 Normalized mean axial velocity $\langle u \rangle / u_B$ at different axial positions **a** over the duct and **b** within the gap for ♦ ● ▲ $c/k_r = 0.1$, ♦ ● ▲ $c/k_r = 0.3$, ◊ ○ △ $c/k_r = 0.5$, and ♦ ● ▲ $c/k_r = 1.0$ in the $z/H = 0.0$-plane. No measurement data were obtained for the near-wall region between $x/k_r = 0.0$ and 3.0 for $c/k_r = 0.1$

windows and the aluminum frame. Furthermore, only 50 000 random samples per measurement point were recorded in the regions $z/k_r > 4.5$ and $z/k_r < -4.5$ due to the low particle density close to the side walls. Additionally, the wall-normal orientation of the longitudinal axis of the measurement volume resulted in low-quality signals in the wall-bounded shear layers in the immediate vicinity of the duct side walls.

3 Results

3.1 Mean velocity field

Distributions of the normalized mean axial and vertical velocities along the duct height and within the gap at different axial positions in both measuring planes are depicted in Fig. 5-Fig. 7. As shown, the mean flow pattern in the duct varied with the clearance-to-rib-height ratio. The mean flow field near the ribs and within the inter-rib region varied differently with c/k_r (Figs. 5, 6 and 7). Variations in axial direction of the $\langle u \rangle$- and $\langle v \rangle$-distributions in the regions $y/k_r > 4.0$ and $y/k_r > 5.0$, respectively, were small for each specific clearance-to-rib-height ratio. Considering the measurement uncertainty, it can be assumed that above the range of $4.0 < y/k_r < 5.0$ the mean velocity field became almost independent of the axial position. The differences in the mean velocity distributions between the measuring planes as well as their significant changes in lateral direction (Fig. 4) were attributed to geometry-induced secondary flows depending on c/k_r.

3.1.1 Geometry-induced secondary flow motion

The clearance-to-rib-height ratio influenced the formation of geometry-induced secondary flows. Hence, variations of c/k_r significantly affected the entire flow field. This subsection therefore highlights the effect of c/k_r on the mean flow field. With the exception of the region close to the rib

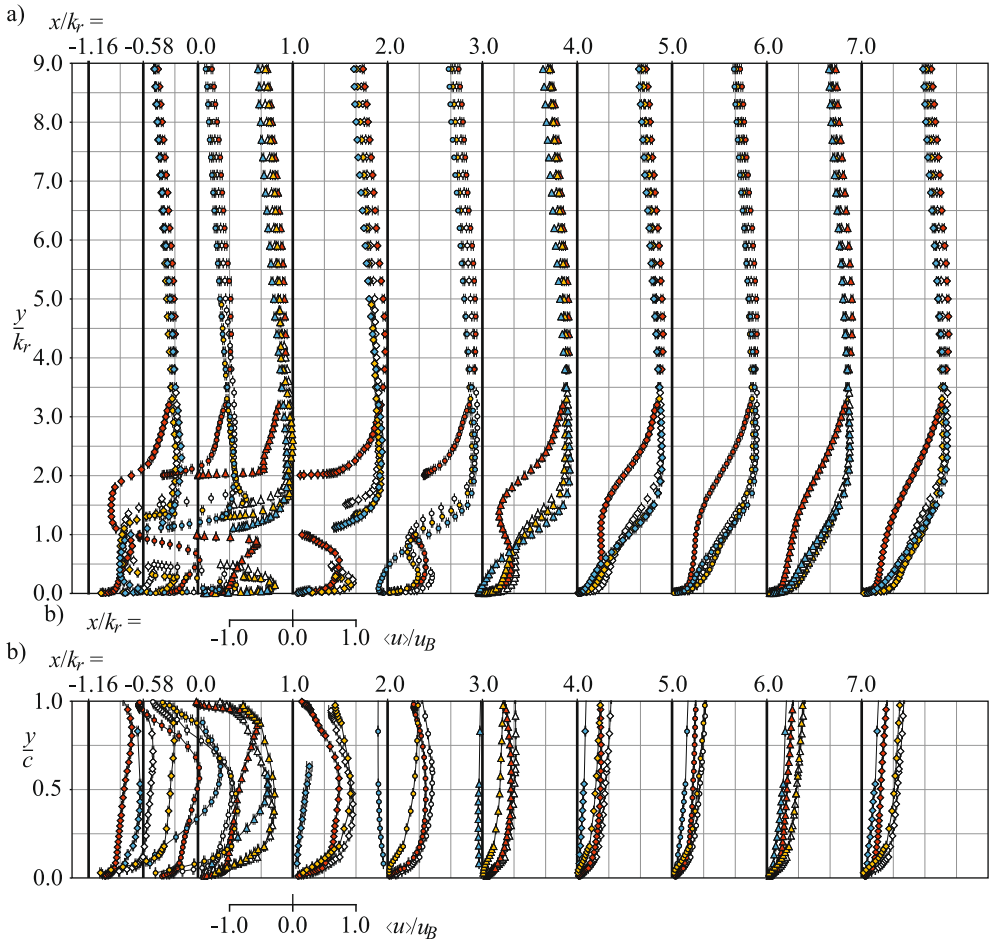

Fig. 6 Normalized mean axial velocity $\langle u \rangle / u_B$ at different axial positions for ♦ ● ▲ $c/k_r = 0.1$, ♦ ● ▲ $c/k_r = 0.3$, ◇ ○ △ $c/k_r = 0.5$, and ♦ ● ▲ $c/k_r = 1.0$ within the $z/H = 0.25$-plane

and near the wall, the negative mean vertical velocity in the duct symmetry plane indicated a downward fluid transport as shown in Fig. 7. The magnitudes of the maximum negative mean vertical velocities above the ribs were similar to those of attached divergent ribs and by far exceeded those of transversely oriented attached ribs (Coletti et al. 2013). Above the rib-roughened wall, $\langle v \rangle$ increased in the direction of the duct side walls and became positive, representing an upward fluid motion as shown in Fig. 4b. The lateral development of $\langle v \rangle$ indicated a substantial variation in vertical and lateral momentum transport depending on c/k_r. The mean velocity distributions in Fig. 7 suggested that the secondary flow field above the detached divergent ribs was similar to that of attached divergent ribs (Gao and Sundén 2004b; Fang et al. 2015; Mahmoodi-Jezeh and Wang 2022), whose time-averaged flow in the axial-normal plane ($y-z$) was governed by a pair of counter-rotating large vortices. The rib inclination relative to the main flow direction caused the fluid to flow downstream and sideways from the rib tip toward the duct side walls. Spatial confinement of the duct forced fluid deflected sideways to flow upward near the duct side walls. This upward motion was accompanied by a reversed fluid motion around the duct symmetry plane due to momentum balancing, thus resulting in the rotational secondary flow. The mean flow pattern above the rib was found for all c/k_r investigated, with downward fluid motion in the $z/H = 0.0$-plane being strongest for $c/k_r = 0.3$ and weakest for $c/k_r = 1.0$. In each case, the effects of secondary flow motion on the mean flow field extended over the entire observation region. According to the zero crossings of $\langle v \rangle$ in Fig. 4b (measuring line in z-direction at $y/k_r = 5.0$ and $x/k_r = 4.0$) and Fig. 7 b, the foci of the two main vortex structures of the secondary flow field were located near the $z/H = 0.25$ plane and above the duct center plane.

Since the fluid was also deflected downward at the windward rib surface, development of secondary flow structures in the gap below the ribs was expected. However, flow velocity in the gap was measured in one dimension only due to the limitations of the field of view of the measuring system and the geometry. This hardly allows any conclusions to be drawn

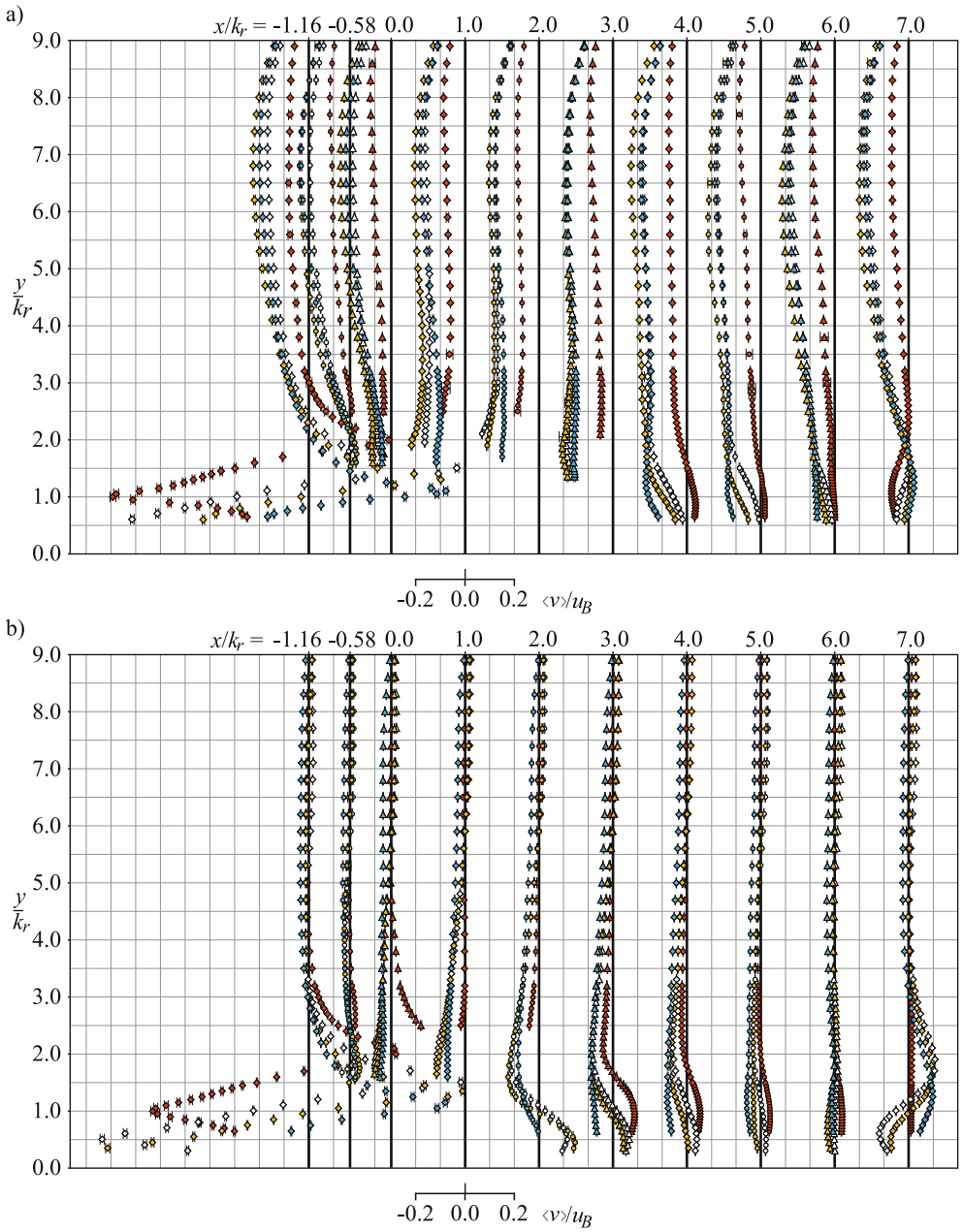

Fig. 7 Normalized mean vertical velocity $\langle v \rangle / u_B$ at different axial positions for ♦ ● ▲ $c/k_r = 0.1$, ♦ ● ▲ $c/k_r = 0.3$, ◇ ○ △ $c/k_r = 0.5$, and ♦ ● ▲ $c/k_r = 1.0$ in the (**a**) $z/H = 0.0$-plane and (**b**) $z/H = 0.25$-plane

with respect to a possible three-dimensional secondary flow below the ribs. Nevertheless, the increase of $\langle v \rangle$ in the region below the rib crest (Fig. 4 ($c/k_r = 0.3$), Fig. 7) as well as the lateral variations of $\langle u \rangle$ in the gap (Figs. 5b and 6b) and the near-wake could be hypothetically attributed to a geometry-induced secondary flow that develops below the rib crest and significantly influences the wake, despite the secondary flow field above.

3.1.2 Mean velocity field close and above the rib

Rib-induced blocking of the duct cross section accelerated the fluid at the windward rib surface and increased the mean velocities as shown in Figs. 5, 6, and 7. In contrast to attached divergent ribs (Fang et al. 2015; Mahmoodi-Jezeh and Wang 2022), the fluid was displaced upward, sideways, and downward. As depicted in Fig. 7, positive and negative peaks of $\langle v \rangle$ occurred in regions close to the upper and lower rib leading edges, respectively. This happened in both measuring planes

for all c/k_r. Of all investigated c/k_r, the $\langle v \rangle$ maximum was lowest for $c/k_r = 1.0$ in both measuring planes (Fig. 7), while $\langle v \rangle$ maxima for the remaining clearance-to-rib-height ratios reached comparable values. The highest mean velocities at the rib leading edge occurred in the $z/H = 0.0$-plane for $c/k_r = 0.5$ and in the $z/H = 0.25$-plane for $c/k_r = 0.3$. Due to lack of measured values in the near-wall region at $x/k_r = -1.155$, it can only be assumed that $\langle v \rangle$ peaks were highest for $c/k_r = 0.3$ or 0.5. The differences between the magnitudes and maxima of $\langle v \rangle$ with c/k_r were attributed to the variations in the near flow field and in the formation of the secondary flow. The downward mean flow above the rib due to the secondary flow field decreased the positive $\langle v \rangle$ and increased the negative $\langle v \rangle$ of the fluid deflected upward and downward, respectively, at the windward rib surface. The latter was also reflected in the slight increase of the local $\langle v \rangle$ maxima due to a reduced downward velocity above the rib ($-1.155 \leq x/k_r \leq 0.0$) in the $z/H = 0.25$-plane compared to the $z/H = 0.0$ plane (Fig. 7).

For turbulent flow in a square duct with transversely oriented attached ribs (Coletti et al. 2013; Mahmoodi-Jezeh and Wang 2020) or detached ribs (Liou et al. 1997) applied on one duct wall, reduced momentum transport near the rib-roughened wall leads to a vertical shift of the local maxima of $\langle u \rangle$ toward the opposite smooth wall and a considerable primary mean shear rate ($\partial \langle u \rangle / \partial y$) across the duct. For the investigated turbulent flow in the square duct rib-roughened by detached divergent ribs, by contrast, fluid downwash due to the secondary flow field caused an intensification of momentum transport near the ribs. This increased $\langle u \rangle$ above the ribs and shifted the local maxima toward the rib-roughened wall (Figs. 5 and 6). Strong shear layers with high velocity gradients developed along the rib crest, whereas the primary mean shear rate was low immediately above the rib. Here, no recirculation zone was found which might be a consequence of the coarse streamwise resolution of measurement points or recirculating flow within a very thin region that was not captured by the measurements. The mean axial velocity peaks in the upper shear layer were increased compared to transversely oriented detached ribs in single configuration (Wang and Tan 2008) or array configuration (Ahn and Lee 2010) and were similar to those of divergent attached ribs (Fang et al. 2017). For varying c/k_r, the global $\langle u \rangle$ maxima occurred above the rib ($x/k_r = -0.58$) and in the immediate rib wake ($x/k_r = 0.0$ and 1.0) in the $z/H = 0.0$-plane. For both measuring planes it was found that the closer the $\langle u \rangle$ maximum was located to the rib, the higher was its magnitude was. Downward mean fluid motion above the rib due to the secondary flow field caused the development of a very thin shear layer along the rib crest within the $z/H = 0.0$-plane. The vertical distances of global $\langle u \rangle$ maxima from the rib crest were $0.1 < \Delta y < 0.3$ for $c/k_r = 0.3$ and 0.5 and increased with decreasing and increasing c/k_r. With a reduction of $\langle v \rangle$ in lateral direction, the local $\langle u \rangle$ maxima moved away from the rib-roughened wall as indicated by the different distributions of $\langle u \rangle$ at each axial position x/k_r and shown in the $z/H = 0.0$- and $z/H = 0.25$-planes in Figs. 5 and 6. The maxima of $\langle u \rangle$ in the $z/H = 0.25$-plane also occurred above the rib ($x/k_r = -0.58$) and in the immediate wake of the ribs ($x/k_r = 0.0$ and 1.0).

3.1.3 Mean velocity field close to and below the rib

The flow field in the gap below the rib determines the development of the wake configuration. High fluid acceleration near the windward rib surface resulted in the formation of strong shear layers with high velocities at the rib bottom surface and at the bottom duct wall for $c/k_r \geq 0.3$ (Figs. 5 and 6). The $\langle u \rangle$ distributions within the gap varied with c/k_r and z/H, as depicted in Figs. 5b and 6b. For $c/k_r = 0.3$ and 0.5, the mean axial velocities and their trends (at $x/k_r = -0.58$ and 0.0) were similar to those of $c/k_r = 1.0$ (at $x/k_r = -0.58$), but at higher axial velocity levels. This was different for the flow below a transversely oriented detached square cylinder, where the mass flow in the gap decreased with increasing proximity of the rib to the wall (Addai et al. 2022; Park et al. 2001) and was attributed to the strong secondary flow field. It was assumed that for the detached divergent rib with $c/k_r = 0.3$ and 0.5, downward fluid transport by secondary flow extended from the duct core to the near-wall region in the inter-rib spacing as reflected by the negative mean vertical velocity in Fig. 7, which leads to an increase in the mass flow rate.

For the smallest gap height with $c/k_r = 0.1$, the velocity profile became more convex and the velocity level decreased. This effect was related to the decrease of the mass flow rate in the gap due to a reduction of the gap height (the Reynolds numbers in the gap were $\mathrm{Re}_c = u_{mc} \cdot c/\nu = 450$, 1683, 2881, and 3973 for $c/k_r = 0.1, 0.3, 0.5$, and 1.0, respectively, in the $z/H = 0.0$-plane, where u_{mc} is the mean axial velocity averaged over the gap). Convex velocity profiles were observed for single transversely oriented ribs at higher clearance-to-rib-height ratios (Park et al. 2001) ($c/k_r = 0.3$). They were accompanied by a suppression of periodic vortex shedding from the rib. It can be assumed that enhanced fluid transport to the inter-rib spacing of divergent ribs caused the mass flow rate in the gap to persist at a higher level as wall proximity increased. The inflection point of the mean velocity profile at $x/k_r = -0.58$ for $c/k_r = 0.1$ in Fig. 5 b suggested the development of recirculation regions due to flow separation at the lower bottom duct wall, which was not found for $c/k_r \geq 0.3$.

The asymmetry of the $\langle u \rangle$ distributions in the $z/H = 0.0$-plane relative to the gap center plane with more pronounced velocity gradients and velocity maxima close to the lower rib surface indicated upward fluid motion below the rib in

the $z/H = 0.0$-plane as a result of a geometry-induced fluid motion in the gap. Although the Reynolds numbers in the gap Re_c varied only slightly between the two measuring planes ($Re_c = 442$, 1802, 2828, and 3211 for $c/k_r = 0.1$, 0.3, 0.5, and 1.0, respectively, in the $z/H = 0.25$-plane), the $\langle u \rangle$ distributions differed significantly. The velocity profiles were more convex in the $z/H = 0.25$-plane. Locations of local maxima $\langle u \rangle$ shifted downward and shear rates at $x/k_r = -0.58$ were less intense. For $c/k_r = 1.0$, flow detached along the lower rib surface between the lower rib leading edge and the rib center without reattaching further downstream (Fig. 6 b). No flow detachments were detected along the lower and upper rib surfaces for the other clearance-to-rib-height ratios.

3.1.4 Wake configuration in the inter-rib spacing

The flow close to the ribs is of major interest when applying ribs as a design tool to enhance heat transfer of thermally highly loaded heat exchanger surfaces, since. As inferred from Figs. 5, 6, 7, 8, and 9, the shear layers forming along the upper and lower rib surfaces separated at the rib trailing edges ($x/k_r = 0.0$) and transformed into two free shear layers behind the upper and lower rib trailing edges. According to the existing literature on flow of a detached transversely oriented square cylinder near a wall (Durão et al. 1991; Bosch et al. 1996; Bailey et al. 2002; Martinuzzi et al. 2003; Wang and Tan 2008; Addai et al. 2022; Panigrahi 2009), an interaction of the shear layers separating at the rib trailing edges and the wall-bounded shear flow might be expected as wall proximity increases. It is assumed that the intensity of the interaction depends on the geometry-induced fluid motion above and below the rib, which varies with the clearance-to-rib-height ratios as indicated by the lateral variations of $\langle v \rangle$ in Fig. 4b.

Compared to a detached transversely oriented square cylinder near a wall with comparable wall clearance-to-rib-height ratios (Wang and Tan 2008), the upper shear layer behind the detached divergent rib developed in axial direction closer to the duct bottom with steeper mean velocity gradients. This is due to the geometry-induced downwash of high-momentum flow from the duct core toward the rib-roughened wall. In addition, the extension of the flow cross section and the associated adverse axial pressure gradient caused a further decrease in the negative vertical velocity immediately behind the rib in the range $1.5 \leq y/k_r \leq 3.0$, see Fig. 7. In contrast to this, vertical spreading of the fluid leaving the gap due to the change in flow cross section is expected to result in positive vertical velocities behind the gap above the lower rib trailing edge for all clearance-to-rib-height ratios (not resolved immediately downstream of the gap). As obvious from Fig. 7, the occurrence and strength of positive mean vertical velocity behind the rib correlated with a clearance-to-rib-height-ratio increase. Upward fluid motion behind the rib was lowest for $c/k_r = 0.1$ and highest for $c/k_r = 1.0$.

For all c/k_r investigated, the large recirculation region between the leeward rib surface and the bottom duct wall occurring for attached ribs due to the reattachment of the shear layer separated from the upper rib trailing edge (Fang et al. 2017) was not found. Interaction of the upper and lower free shear layers behind the rib at $x/k_r = 1.0$ was excluded based on the mean velocity distributions in Figs. 5, 6 and 7.

As inferred from the negative mean axial velocities for $c/k_r = 0.1$ close to the bottom duct wall in both measurement planes shown in Figs. 5b and 6b, a three-dimensional recirculation region was formed in the region $1.0 < x/k_r < 5.0$ within the $z/H = 0.0$-plane and in the region $1.0 < x/k_r < 4.0$ at $y/k_r < 0.5$ within the $z/H = 0.25$-plane. Similar to a detached transversely oriented square cylinder with $c/k_r \leq 0.25$ (Durão et al. 1991; Shi et al. 2010b) (see Fig. 1 b), the wall-bound shear flow was assumed to detach from the bottom duct wall with the upward motion (Fig. 7) of the lower free shear layer due to the axial adverse pressure gradient. The momentum flux resulting from the flow exiting the gap was too weak to overcome the axial pressure gradient and the vorticity ($\partial\langle u \rangle/\partial y - \partial\langle v \rangle/\partial x$). The mean shear rate of the lower free shear layer was assumed to be insufficient for coupling with the upper free shear layer. Vortical structures formed in the upper shear layer remained almost undisturbed further downstream, while the shear layer was stretched longitudinally and surrounded the thin recirculation region below. After reattachment, a wall-bounded shear layer developed against the adverse pressure gradient (which was indicated by the dips of the velocity profiles downstream the reattachment points, see Figs. 5a and 6a). The smaller vertical extent of the recirculation region compared to a detached transversely oriented square cylinder (Shi et al. 2010a) results from secondary flow motion that pushes the upper shear layer toward the bottom duct wall.

For $c/k_r \geq 0.3$, the high flow velocities in the gap enabled the exiting fluid to flow against the rising pressure gradient without detachment from the bottom duct wall. The mean flow field configurations within the inter-rib spacing for $c/k_r = 0.1$ and for $c/k_r \geq 0.3$ differed fundamentally, while the mean velocity distributions in the rib wake for $c/k_r = 0.3$, 0.5, and 1.0 showed similar trends. Due to the oppositely directed fluid motion above and below the rib trailing edges, the separated free shear layers tended to interact further downstream for $c/k_r \geq 0.3$, if not already diffused as shown for a detached transversely oriented square cylinder with small clearances (Wang and Tan 2008). In general, the decrease in local mean velocity gradients and local mean velocity maxima in the vicinity of the bottom duct wall shown for $1.0 \leq x/k_r \leq 3.0$ in Figs. 5 and 6 can be attributed to the mixing of upper and lower free shear layers and their diffusion downstream, respectively. It was concluded that the free

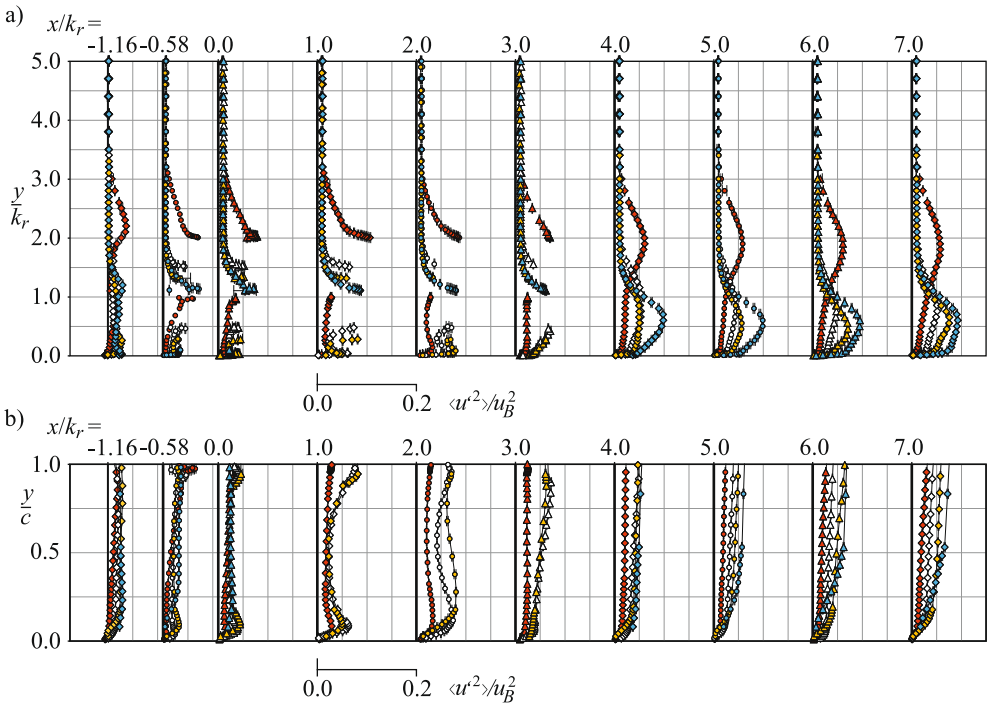

Fig. 8 Normalized axial Reynolds normal stress $\langle u'^2 \rangle / u_B^2$ at different axial positions (**a**) over the duct and (**b**) within the gap for ♦ ● ▲ $c/k_r = 0.1$, ♦ ● ▲ $c/k_r = 0.3$, ◊ ○ △ $c/k_r = 0.5$, and ♦ ● ▲ $c/k_r = 1.0$ in the $z/H = 0.0$-plane

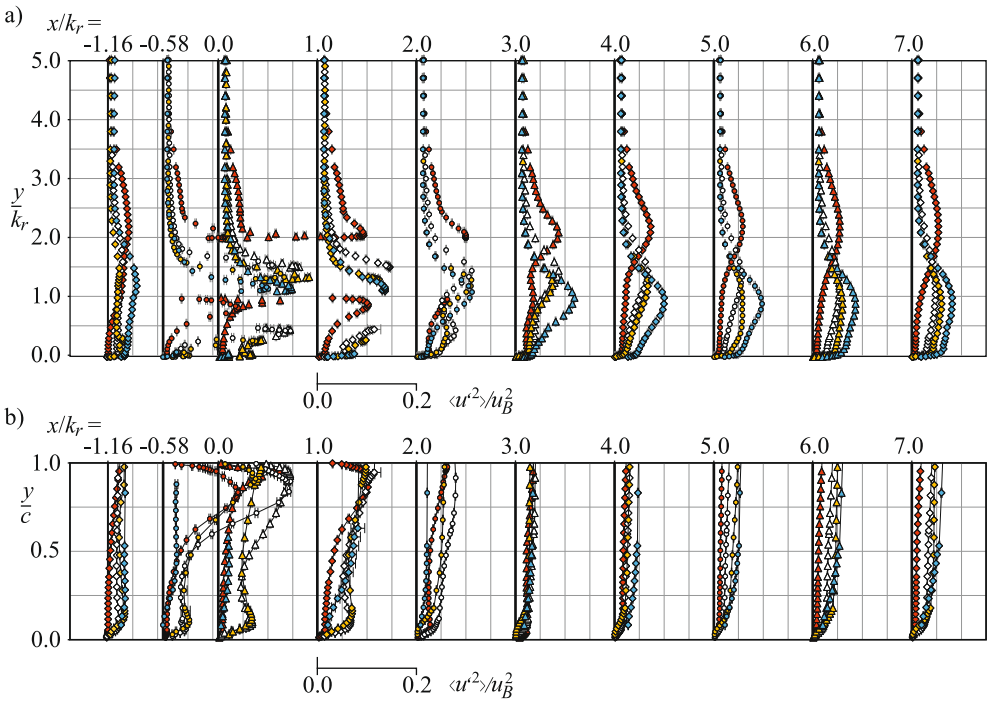

Fig. 9 Normalized axial Reynolds normal stress $\langle u'^2 \rangle / u_B^2$ at different axial positions (**a**) over the duct and (**b**) within the gap for ♦ ● ▲ $c/k_r = 0.1$, ♦ ● ▲ $c/k_r = 0.3$, ◊ ○ △ $c/k_r = 0.5$, and ♦ ● ▲ $c/k_r = 1.0$ in the $z/H = 0.25$-plane

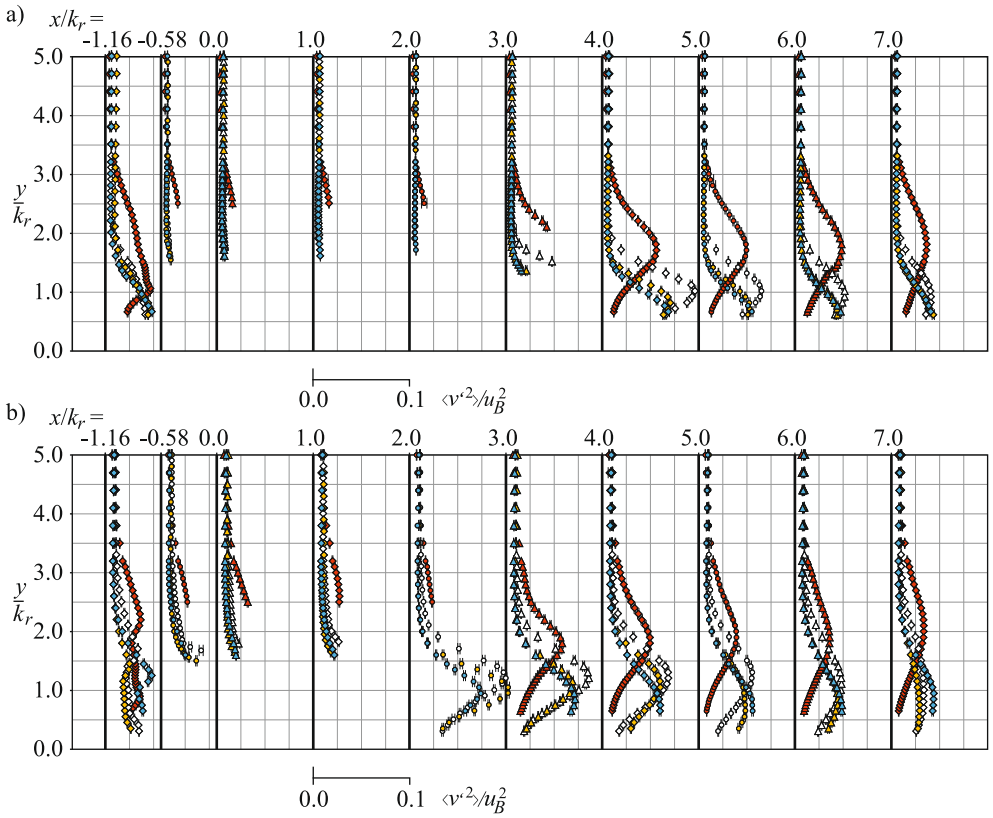

Fig. 10 Normalized vertical Reynolds normal stress $\langle v'^2 \rangle / u_B^2$ at different axial positions for ♦ ● ▲ $c/k_r = 0.1$, ♦ ● ▲ $c/k_r = 0.3$, ◊ ○ △ $c/k_r = 0.5$, and ♦ ● ▲ $c/k_r = 1.0$ in the (**a**) $z/H = 0.0$-plane and (**b**) $z/H = 0.25$-plane

shear layer that separated from the lower rib trailing edge vanished further downstream. The three shear layers (free upper, free lower, and wall-bounded) initially occurring in the inter-rib region converged to one wall-bounded shear layer. The consistently positive mean axial velocity at the bottom duct wall for $c/k_r \geq 0.3$ indicated no permanent reattachment of the free shear layers and no further flow detachment in the inter-rib spacing. However, the inflection point profiles for $\langle u \rangle$ in the immediate vicinity of the wall for $c/k_r = 0.3$ at $x/k_r = 2.0$ within the $z/H = 0.25$-plane in Fig. 6 suggested a possible flow detachment between $x/k_r = 1.0$ and $x/k_r = 2.0$, which was not resolved due to the coarse axial spatial resolution. Despite the similarities for $c/k_r \geq 0.3$, the mean velocity distributions revealed significant differences for varying c/k_r. For $c/k_r = 1.0$, compared to $c/k_r = 0.3$ and 0.5, the lower mean vertical velocity was assumed to prevent the upper free shear layers from interacting intensively with the wall and enable a less disturbed development of both shear layers further downstream. This is consistent with the dip in the distributions of $\langle u \rangle$ for $c/k_r = 1.0$ that indicates a longer persistence of the lower free shear layer in the inter-rib spacing further downstream than for $c/k_r < 1.0$. It is also in agreement with the almost consistent mean axial velocity distribution close to the wall.

In front of the subsequent rib ($x/k_r = 7.0$), $\langle v \rangle$ peaks developed in the $z/H = 0.25$-plane due to the flow displacement by the rib. The marginal $\langle v \rangle$ increase for $c/k_r = 1.0$ was attributed to the reduced blocking effect upstream of the rib as a result of the comparatively large clearance.

3.2 Reynolds stress distribution

The distributions of the normalized Reynolds normal stresses $\langle u'^2 \rangle / u_B^2$ and $\langle v'^2 \rangle / u_B^2$ as well as of the Reynolds shear stress $-\langle u'v' \rangle / u_B^2$ in both measurement planes are shown in Figs. 8, 9, 10, 11 and 12. Figure 12 shows the lateral development of the Reynolds stresses. The high mean shear rates and vorticity in the shear layers developing along the rib surfaces and the unsteady wake led to a significant increase of the Reynolds stresses near the rib-roughened wall as well as close to the smooth duct side walls. Considering the results for attached divergent ribs (Fang et al. 2015, 2017), it was assumed that secondary fluid motion resulted in a clustering of high-energy turbulent structures close to the smooth side walls and within the inter-rib spacing. The absence of high-energy turbulent structures and primary mean velocity shear within both measurement planes above the rib resulted in low turbulence kinetic energy and Reynolds normal stress production.

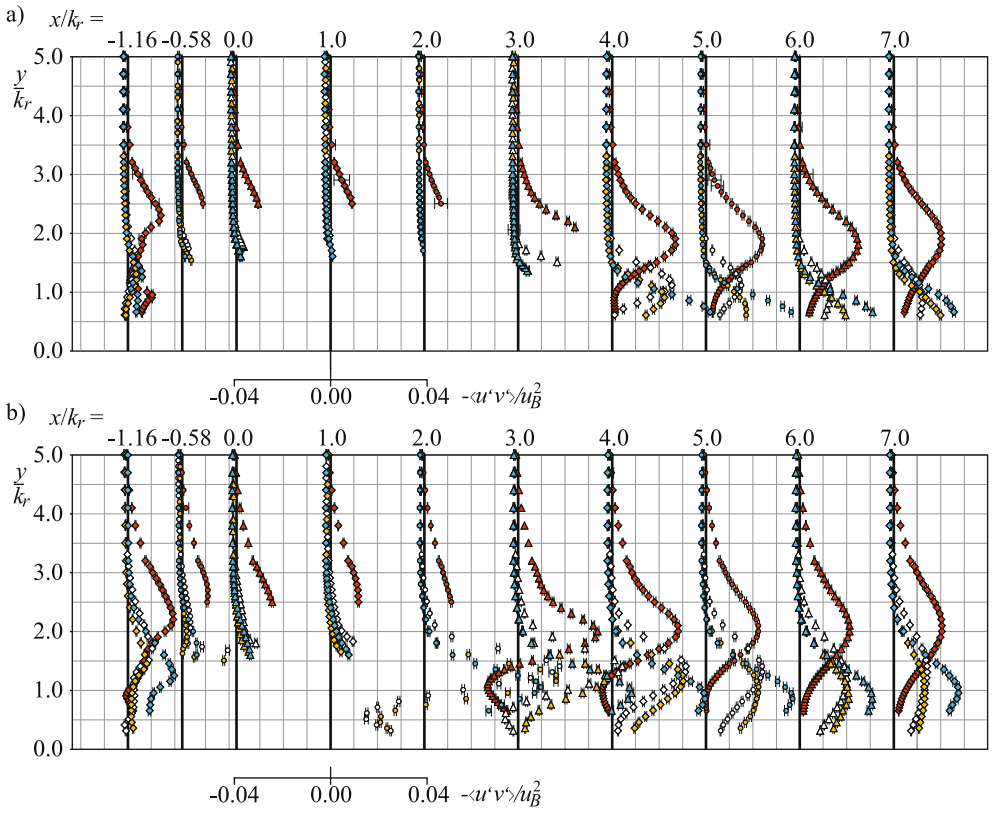

Fig. 11 Normalized Reynolds shear stress $-\langle u'v'\rangle/u_B^2$ at different axial positions for ♦ ● ▲ $c/k_r = 0.1$, ♦ ● ▲ $c/k_r = 0.3$, ◇ ○ △ $c/k_r = 0.5$, and ♦ ● ▲ $c/k_r = 1.0$ in the (**a**) $z/H = 0.0$-plane and (**b**) $z/H = 0.25$-plane

Reynolds stresses almost vanished between $y/k_r = 3.0$ for $c/k_r \leq 0.5$ or $y/k_r = 3.5$ for $c/k_r = 1.0$ and the near-wall region close to the upper smooth duct wall (not shown). Vertical growth of the region with significant Reynolds stress variations with increasing c/k_r was caused by the increasing penetration of the ribs into the flow field with increasing wall distance and by variations in the three-dimensional flow field with varying c/k_r. In general, the differences in the mean flow configuration for varying c/k_r were reflected by the distributions of the Reynolds stresses. The distributions for $c/k_r = 0.3$ and 0.5 were similar, but deviated from the different distributions of $c/k_r = 0.1$ and $c/k_r = 1.0$.

3.2.1 Reynolds stresses close to the rib

The axial Reynolds normal stress increased near the upper and lower rib surfaces. Considerable differences were found in the measuring planes, with $\langle u'^2\rangle$ maxima being much higher (2.8, 6.2, 5.1, and 3.1 times higher for $c/k_r = 0.1$, 0.3, 0.5, and 1.0) within the $z/H = 0.25$-plane than within the 0.0-plane. The global maxima of the axial Reynolds normal stress occurred in the shear layer along the rib crest ($x/k_r = -0.58$ and 0.0) within the $z/H = 0.25$-plane, while the highest $\langle u'^2\rangle$ peaks occurred in the wake within the $z/H = 0.0$-plane.

The higher axial Reynolds normal stress in the upper and lower shear layers along the rib surfaces in the $z/H = 0.25$-plane compared to the $z/H = 0.0$-plane was attributed to lateral fluid motion induced by secondary flow. Turbulent flow structures formed in the vicinity of the upper and lower rib tip regions and within the shear layer along the rib surface near the duct symmetry plane were assumed to be deflected laterally as a result of the geometry-induced lateral flow velocity and fluid deflection caused by the fluid impingement onto the rib surfaces, as sketched in Fig. 13. Therefore, the density of turbulent flow structures contributing substantially to the production of $\langle u'^2\rangle$ was comparatively low in regions close to the $z/H = 0.0$-plane at $x/k_r = 0.0$. $\langle u'^2\rangle$ increased in the shear layer within the $z/H = 0.25$-plane due to high primary mean shear rate and the turbulent flow structures developing during the shear layer formation process or advected laterally from the region of the duct symmetry plane. Axial-lateral motion of the flow structures was supposed to increase the magnitude of the axial-lateral shear stress $\langle u'w'\rangle$. Combined with the geometry-induced lateral mean axial velocity gradient (Fig. 4), the production term

$-\langle u'w'\rangle \partial\langle u\rangle/\partial z$ would contribute significantly to the axial Reynolds stress within the $z/H = 0.25$-plane.

Compared to $c/k_r \geq 0.3$, $\langle u'^2\rangle$ was low for $c/k_r = 0.1$ in the gap. This was due to the reduced mass flow for very small gap heights and the resulting suppression of a strong primary mean velocity shear rate and decay of velocity fluctuations by viscosity damping. As the measurement resolution of vertical velocity was limited spatially by the experimental setup, vertical Reynolds normal stresses and Reynolds shear stress above the ribs were not resolved in the vicinity of the rib upper and lower surface.

3.2.2 Reynolds stresses in the inter-rib spacing

High velocity gradients and intense velocity fluctuations within the shear layers separated at the rib trailing edges caused high streamwise Reynolds normal stresses in the wake. The position of the local $\langle u'^2\rangle$ maxima found in both measurement planes coincided with the position of the inflection points of the primary mean velocity shear rate $\partial\langle u\rangle/\partial y$ (Figs. 5 and 6a) and the local $-\langle u'v'\rangle$ maxima (Fig. 11). Consequently, the mean position of the free shear layers corresponded roughly to that of axial Reynolds stress peaks (Ahn and Lee 2010; Liou et al. 1997). At $x/k_r = 1.0$, two local maxima of $\langle u'^2\rangle$ were identified behind the trailing edges for all clearance-to-rib-height ratios investigated (Figs. 8 and 9). In contrast to a transversely oriented cylinder detached from a wall (Addai et al. 2022), the upper $\langle u'^2\rangle$ peak exceeded the lower $\langle u'^2\rangle$ peak due to the more intense shear layer along the rib crest and the comparably small vorticity of the lower shear layer. As inferred from the local $\langle u'^2\rangle$ maxima for $x/k_r \geq 3.0$ in Figs. 8 and 9, the two free shear layers transformed into one free shear layer while moving downstream due to the interaction of their flow structures in the wake or diffusion of the lower shear layer. Finally, they fused with the attached shear layer.

Similar to turbulent flow in square ducts rib-roughened by attached divergent ribs (Fang et al. 2017; Mahmoodi-Jezeh and Wang 2022), the high negative vertical mean velocity in the $z/H = 0.0$-plane displaced the upper shear layer into the inter-rib spacing. Highest Reynolds stresses in the wake occurred at the leeward region with their maxima decreasing downstream. For $c/k_r \leq 0.5$, the downstream shear layer expanded toward the bottom duct wall, with the local $\langle u'^2\rangle$ maxima being located below the axial rib center line for $x/k_r \geq 4.0$. The higher mean vertical velocity above and the positive vertical mean velocities below the rib crest for $c/k_r = 1.0$ led to propagation of the free shear layers further downstream rather than to the bottom duct wall. With the $\langle v\rangle$ increase in the lateral direction, the flow separating at the upper rib trailing edges was less intensively displaced downward, as can be seen from the upward shift of the local $\langle u'^2\rangle$ maxima in Fig. 9 compared to Fig. 8. The $\langle u'^2\rangle$ distri-

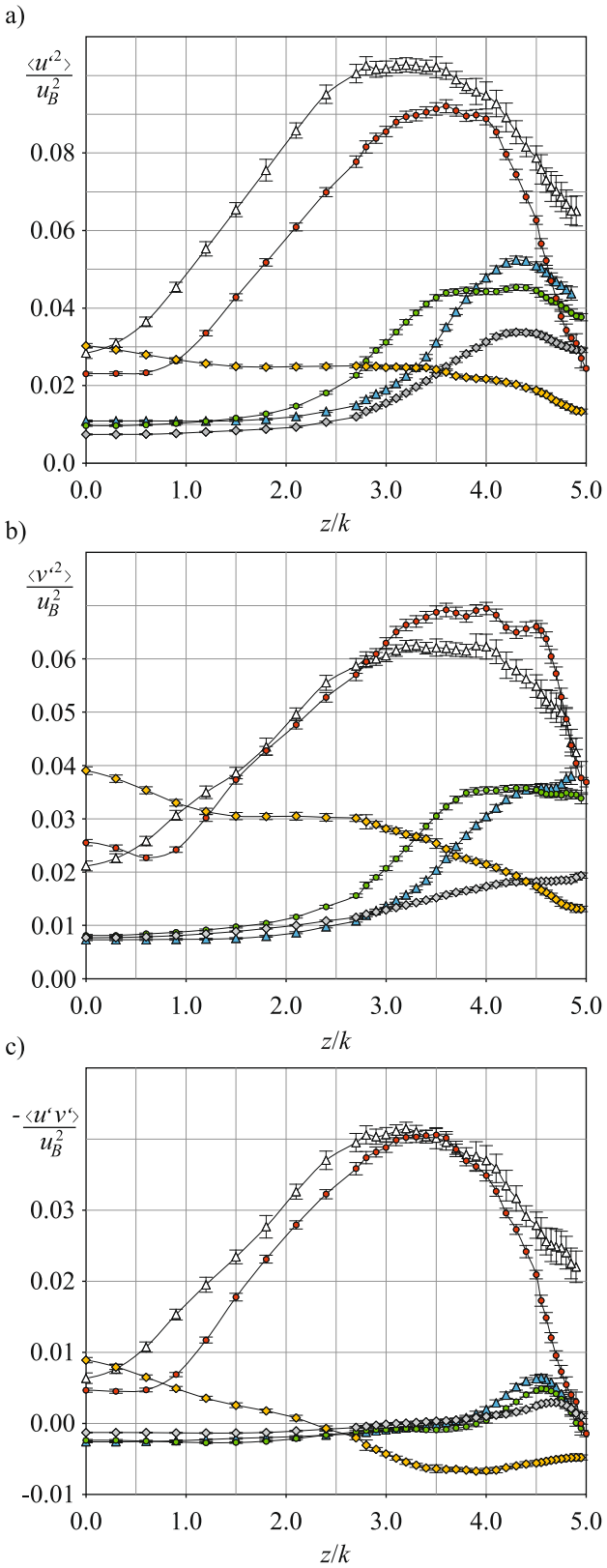

Fig. 12 Normalized (**a**) axial Reynolds normal stress $\langle u'^2\rangle/u_B^2$, (**b**) vertical Reynolds normal stress $\langle v'^2\rangle/u_B^2$, and (**c**) Reynolds shear stress $-\langle u'v'\rangle/u_B^2$ measured along lines parallel to the z-axis at $x/k_r = 4.0$, $y/k_r = 1.3$ for △ $c/k = 0.1$, ● 0.3, and ♦ 1.0 and at $x/k_r = 4.0$, $y/k_r = 5.0$ for ▲ $c/k_r = 0.1$, ● 0.3, and ♦ 1.0

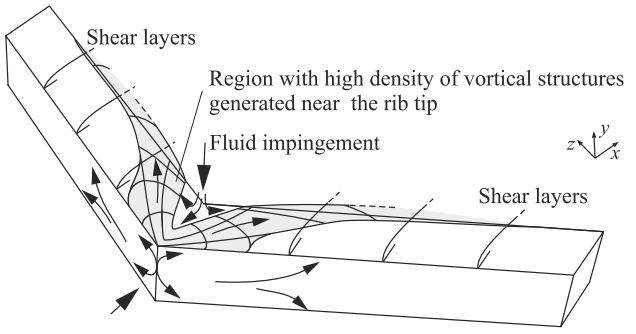

Fig. 13 Sketch of vortical structures generated at the upper rib tip and transported sideways due to the lateral fluid motion and the fluid impingement caused by the secondary flow

bution for $c/k_r = 0.1$ in the wake differed from that for $c/k_r \geq 0.3$. The comparatively high axial Reynolds normal stress for $c/k_r = 0.1$ at $x/k_r \geq 4.0$ in the $z/H = 0.0$-plane and at $x/k_r \geq 3.0$ in the $z/H = 0.25$-plane resulted from the undisturbed longitudinal expansion of the upper shear layer that enclosed the thin recirculation region.

The Reynolds stresses increased in lateral direction as shown in Fig. 12. The Reynolds stress peaks behind the rib ($x/k_r = 4.0$, $y/k_r = 1.3$) for $c/k_r \leq 0.5$ were attributed to an accumulation of turbulent flow structures generated at the rib, pushed into the inter-rib spacing behind the trailing edge, and were convected sideways by lateral fluid motion. Furthermore, the above-mentioned lateral removal of turbulent flow structures generated at the rib near the duct symmetry plane (Fig. 13) resulted in comparable low Reynolds stresses. For $c/k_r = 1.0$, the Reynolds stress peaks were located above the axially oriented rib center line due to $\langle v \rangle$ increase which explained the decrease in the Reynolds stresses in lateral direction at $x/k_r = 4.0$ and $y/k_r = 1.0$ in Fig. 12. The increase in the Reynolds stress close to the smooth side walls in the duct core pointed to a streamwise-vertical convection of the high-energy turbulent vortex structures clustering near the smooth side walls above the rib at the leeward side (Fang et al. 2017) by secondary flow.

Only one local maximum at each axial position was found for the vertical Reynolds normal stress $\langle v'^2 \rangle$. It was located around the axially oriented rib center line in the $z/H = 0.0$-plane and slightly below the rib crest in the $z/H = 0.25$-plane. The $\langle v'^2 \rangle$ peaks decreased in lateral direction as shown in Fig. 10a and b, although the Reynolds stress distribution in lateral direction in Fig. 12 suggested the contrary as a result of the highly three-dimensional flow field. Maxima $\langle v'^2 \rangle$ were measured in the wake at axial positions closest to the rib. In general, the $\langle v'^2 \rangle$ in the wake was lower than for a detached transversely oriented square cylinder with $c/k_r \geq 0.5$, where both free shear layers formed a Kármán vortex street (Durão et al. 1991; Bosch et al. 1996). $\langle v'^2 \rangle$ maxima were comparable to those of attached divergent ribs (Mahmoodi-Jezeh and Wang 2022). Both axial and vertical Reynolds normal stresses were of the same order of magnitude as indicated by the Reynolds stress ratios $\langle u'^2 \rangle / \langle v'^2 \rangle$ in Fig. 14, but they were far away from unity near the ribs and in the wake. For $c/k_r \geq 0.3$ in the regions between $x/k_r = 4.0$ and 6.0 in the $z/H = 0.0$-plane and between $x/k_r = 3.0$ and 5.0 in the $z/H = 0.25$-plane, $\langle v'^2 \rangle$ slightly exceeded $\langle u'^2 \rangle$. For $c/k_r = 0.1$, the vertical Reynolds stress was smaller than the axial Reynolds stress at each measurement position. Here, the intense primary mean velocity shear rate and the increased Reynolds shear stress-$\langle u'v' \rangle$ in the upper shear layer formed the dominate production term for the axial Reynolds normal stress. The increase in $\langle v'^2 \rangle$ was assumed to predominately result from energy redistribution by pressure–velocity interaction, since the main production term $\langle v'^2 \rangle \partial \langle v \rangle / \partial y$ for the vertical Reynolds normal stress was comparably small. Thus, the ratio of both Reynolds normal stresses was $\langle u'^2 \rangle / \langle v'^2 \rangle > 1.0$ for a large part of the inter-rib spacing.

Similar to the axial Reynolds normal stress, the magnitudes of the Reynolds shear stress increased in the shear layers, while they disappeared in the flow field above the rib. The $-\langle u'v' \rangle$ increase was primarily caused by the motion of turbulent flow structures originating from the shear layers. The development of $-\langle u'v' \rangle$ for $c/k_r \geq 0.3$ coincided with the development of the free shear layers downstream similar to detached transversely oriented square cylinders (Wang and Tan 2008). Reynolds shear stress peaks were located below the rib crest in the inter-rib spacing due to the downwash of turbulent flow structures by secondary flow in the $z/H = 0.0$-plane. With increasing vertical spreading of turbulent flow structures in the lateral direction, the local $-\langle u'v' \rangle$ maxima and minima of the Reynolds shear stress shifted slightly away from the rib-affected wall. Maxima and minima of $-\langle u'v' \rangle$ were measured in the wake at $x/k_r = 2.0$ and $x/k_r = 3.0$ at the height of the rib trailing edges in the $z/H = 0.25$-plane for $c/k_r \geq 0.3$. Values decreased downstream, similar to the $-\langle u'v' \rangle$ distributions for free shear layers in the wake of a rectangular cylinder (Nakagawa et al. 1999a).

For $c/k_r = 0.1$, only one $-\langle u'v' \rangle$ maximum per axial position was found, slightly below the rib crest. In contrast to detached transversely oriented square cylinders, the Reynolds shear stress maxima for $c/k_r = 0.1$ were higher than for larger clearance-to-rib-height ratios. Although the distribution of $-\langle u'v' \rangle$ was not resolved completely down to the wall, it was hypothetically deduced from the measured values that $-\langle u'v' \rangle > 0$ for $c/k_r = 0.1$ in the wake at $x/k_r \geq 4.0$ in the $z/H = 0.0$-plane and at $x/k_r \geq 2.0$ in the $z/H = 0.25$-plane. This is consistent with the absence of $-\langle u'v' \rangle < 0$ for attached ribs (Addai et al. 2022; Fang et al. 2017) where only the shear layer separated from the upper rib trailing edge dominates the wake.

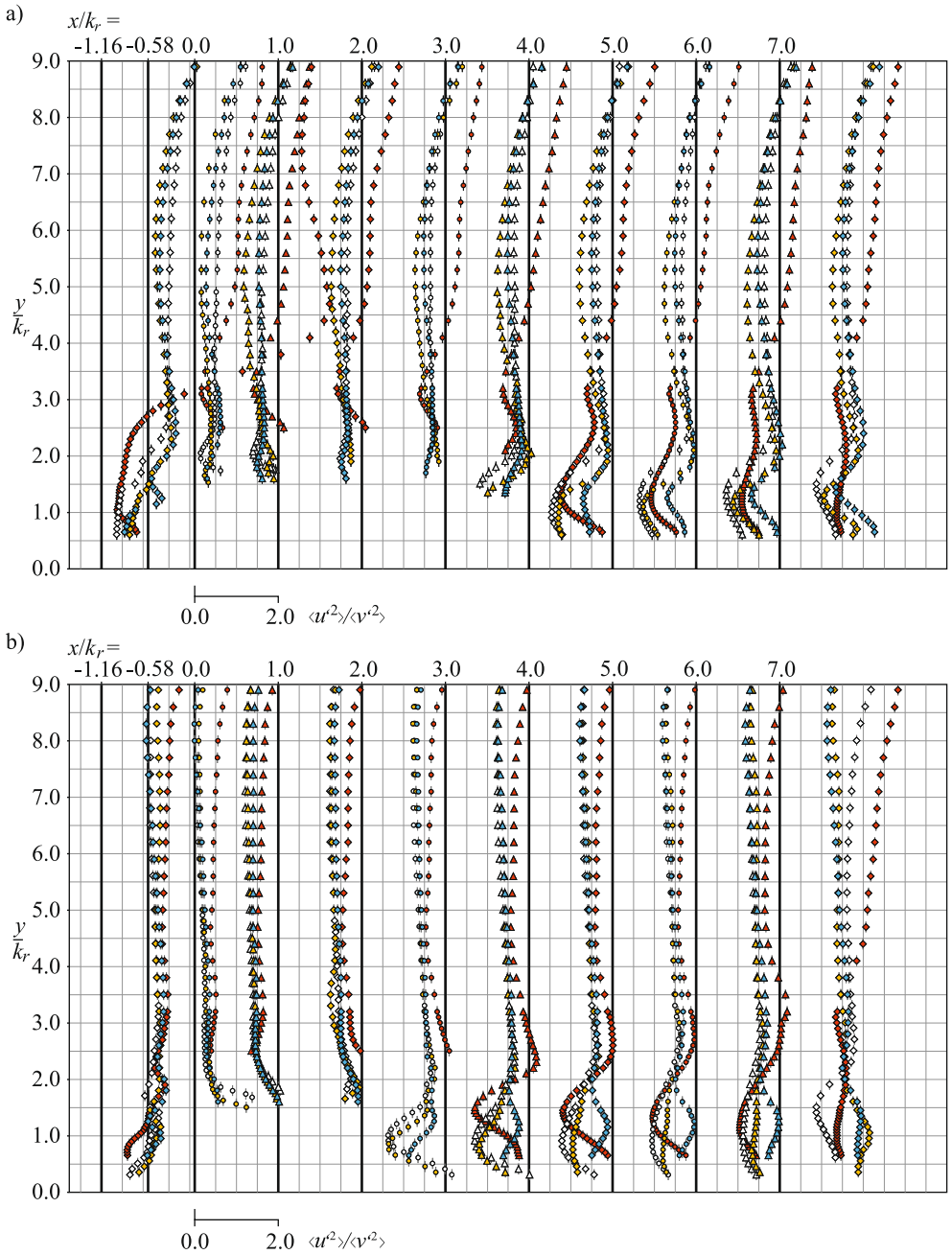

Fig. 14 Reynolds stress ratio $\langle u'^2\rangle/\langle v'^2\rangle$ at different axial positions for ♦ ● ▲ $c/k_r = 0.1$, ♦ ● ▲ $c/k_r = 0.3$, ◊ ○ △ $c/k_r = 0.5$, and ♦ ● ▲ $c/k_r = 1.0$ within the (**a**) $z/H = 0.0$-plane and (**b**) $z/H = 0.25$-plane

3.3 Triple velocity correlations

Turbulent transport of Reynolds stresses associated with the occurrence of fluctuating large-scale flow structures can be analyzed using triple-velocity correlations as shown for rough-wall boundary layers (Andreopoulos and Bradshaw 1981) or rib-roughened duct flows (Mahmoodi-Jezeh and Wang 2020). Their spatial gradients also provide the contribution of turbulent transport to the distributions of the Reynolds stress and the turbulence kinetic energy.

In Figs. 15, 16, 17, 18 and 19, the triple velocity correlations $\langle u'^3\rangle$, $\langle u'^2 v'\rangle$, $\langle u' v'^2\rangle$, and $\langle v'^3\rangle$ normalized by u_B^3 are shown at different axial positions. It is obvious that triple velocity correlations increased near the ribs and varied significantly in a layer close to the wall with a thickness between $2 \times k_r$ and $3 \times k_r$ depending on c/k_r and the measuring plane.

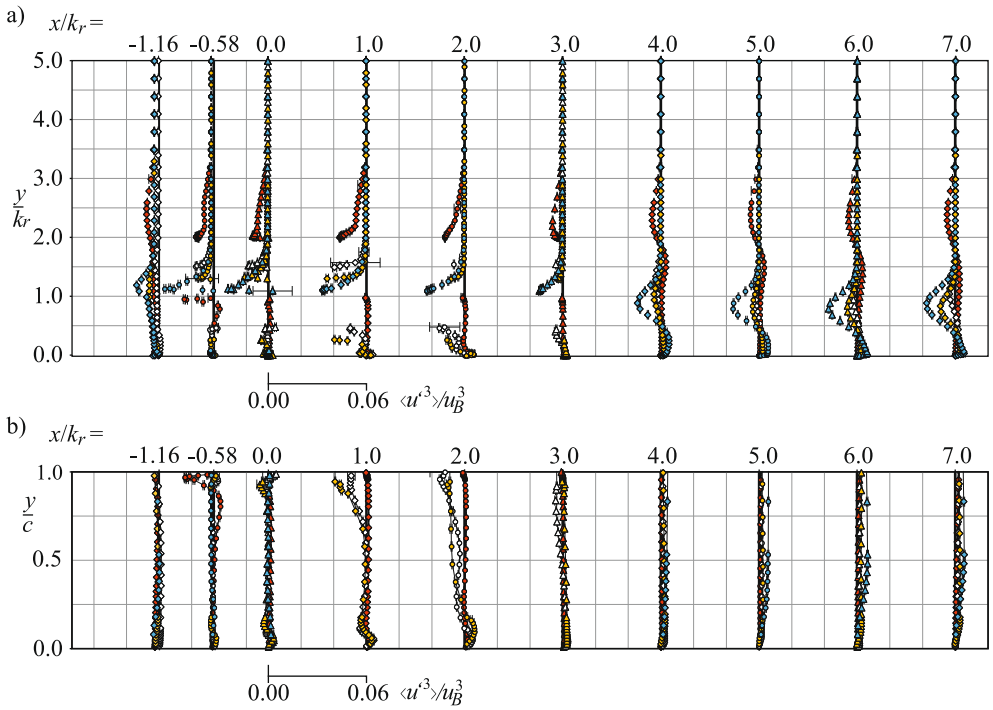

Fig. 15 Normalized triple correlation $\langle u'^3 \rangle / u_B^3$ at different axial positions (**a**) over the duct and (**b**) within the gap for ♦ ● ▲ $c/k_r = 0.1$, ♦ ● ▲ $c/k_r = 0.3$, ◊ ○ △ $c/k_r = 0.5$, and ♦ ● ▲ $c/k_r = 1.0$ within the $z/H = 0.0$-plane

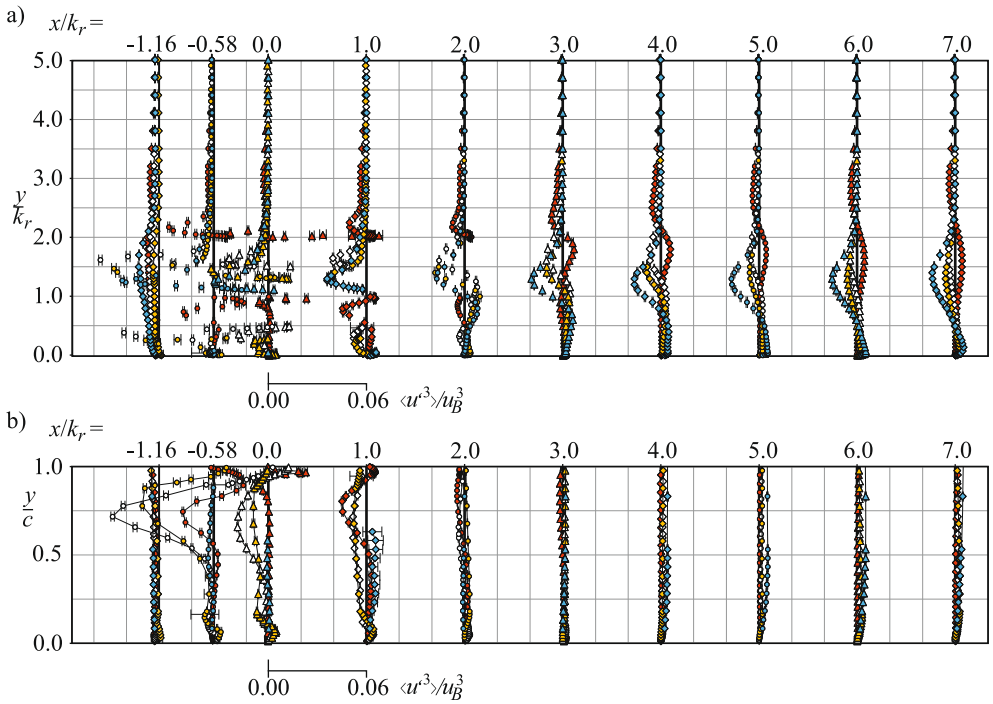

Fig. 16 Normalized triple correlation $\langle u'^3 \rangle / u_B^3$ at different axial positions (**a**) over the duct and (**b**) within the gap for ♦ ● ▲ $c/k_r = 0.1$, ♦ ● ▲ $c/k_r = 0.3$, ◊ ○ △ $c/k_r = 0.5$, and ♦ ● ▲ $c/k_r = 1.0$ within the $z/H = 0.25$-plane

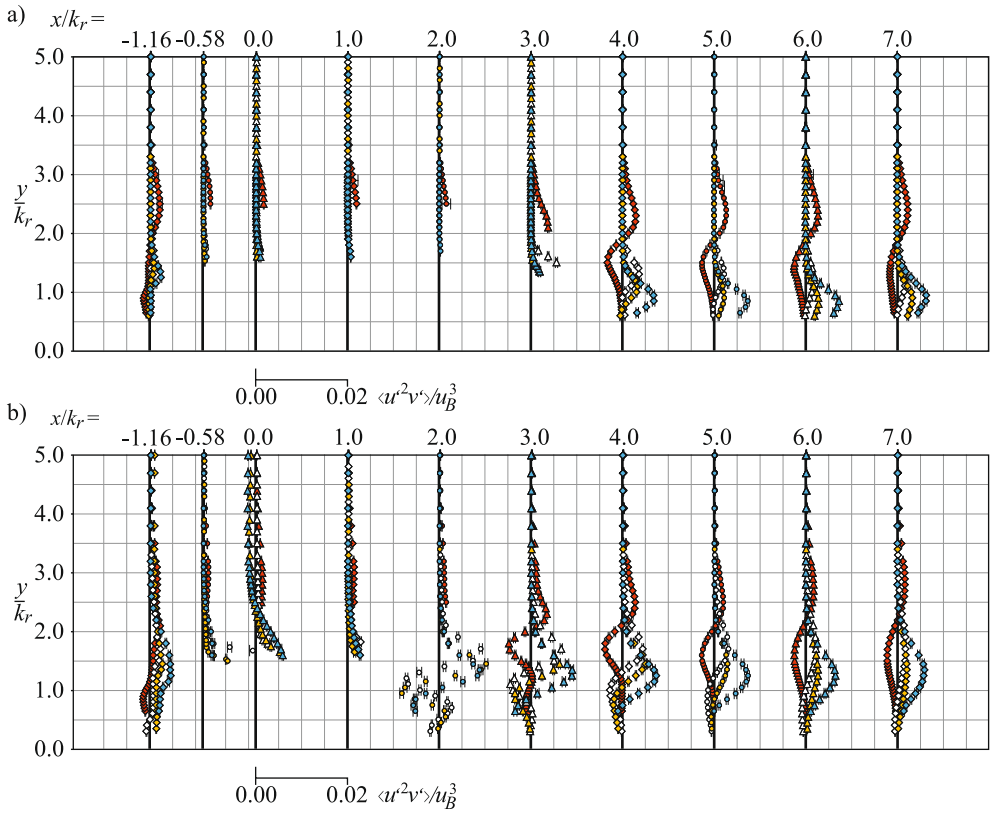

Fig. 17 Normalized triple correlation $\langle u'^2 v' \rangle / u_B^3$ at different axial positions for ♦ • ▲ $c/k_r = 0.1$, ♦ • ▲ $c/k_r = 0.3$, ◇ ○ △ $c/k_r = 0.5$, and ♦ • ▲ $c/k_r = 1.0$ within the (**a**) $z/H = 0.0$-plane and (**b**) $z/H = 0.25$-plane

At a wall distance similar to that of the Reynolds stresses, vertical distributions were independent of the axial position.

3.3.1 Triple velocity correlations close to the rib

Above the upper rib leading edge ($x/k_r = -1.16$), $\langle u'^3 \rangle$ was negative and for $c/k_r = 0.1$ and 1.0, small local negative minima were visible. The coincidence of negative $\langle u'^3 \rangle$ and positive $\langle v'^3 \rangle$ peaks in this region suggested a bursting of flow structures resulting in an increase in the Reynolds shear stress $-\langle u'v' \rangle$ (Fig. 11).

Due to the limitations of the experimental setup, the measurements enabled a valid analysis of the $\langle u'^3 \rangle$ distributions in the immediate vicinity of the ribs only. The triple velocity correlation $\langle u'^3 \rangle$ changed significantly near the detached divergent rib as shown in Figs. 15 and 16. For all c/k_r, $\langle u'^3 \rangle$ dropped to a negative minimum with increasing proximity to the rib crest and then rose again. In the immediate vicinity of the rib surface, the distributions in the two measuring planes differed considerably. Within the $z/H = 0.25$-plane, $\langle u'^3 \rangle$ reached a global positive maximum (at $x/k_r = -0.58$ for $c/k_r \leq 0.5$ and at $x/k_r = 0.0$ for $c/k_r = 1.0$) and subsequently decayed. The positive peaks of $\langle u'^3 \rangle$ in the immediate vicinity of the rib crest in the $z/H = 0.25$-plane reflected the intensive transport of $\langle u'^2 \rangle$ with u' due to axially elongated vortex structures in the shear layers. The S-shaped vertical distribution of $\langle u'^3 \rangle$ with a sign change was measured at the center of the rib ($x/k_r = -0.57$) and at the rib trailing edge ($x/k_r = 0.0$). It is typical of reattaching shear layers on rectangular cylinders (Kumahor and Tachie 2022) or attached square ribs (Ruck and Arbeiter 2022). The absence of the sign change and the positive maximum in the $z/H = 0.0$-plane can be attributed to an attenuation of the turbulent transport of axial elongated flow structures ($\langle u'^2 \rangle$ transported by u') in the thin layer immediately above the wall by downward fluid movement above the rib due to secondary flow. Since the main contribution to triple velocity correlations is known to result from the large turbulent structures, the increase in the $\langle u'^3 \rangle$ minima and maxima at the rib trailing edge in the $z/H = 0.25$-plane supports the previous assumption that vortex structures were transported away in lateral direction due to rib inclination and fluid displacement by secondary flow.

The differences in the triple velocity correlations in lateral direction were also evident in the gap. $\langle u'^3 \rangle$ varied only with $c/k_r = 1.0$ for increasing wall proximity in the $z/H = 0.0$-plane, while $\langle u'^3 \rangle$ showed large negative and positive peaks in the $z/H = 0.25$-plane for $c/k_r \geq 0.3$. For $c/k_r = 0.1$,

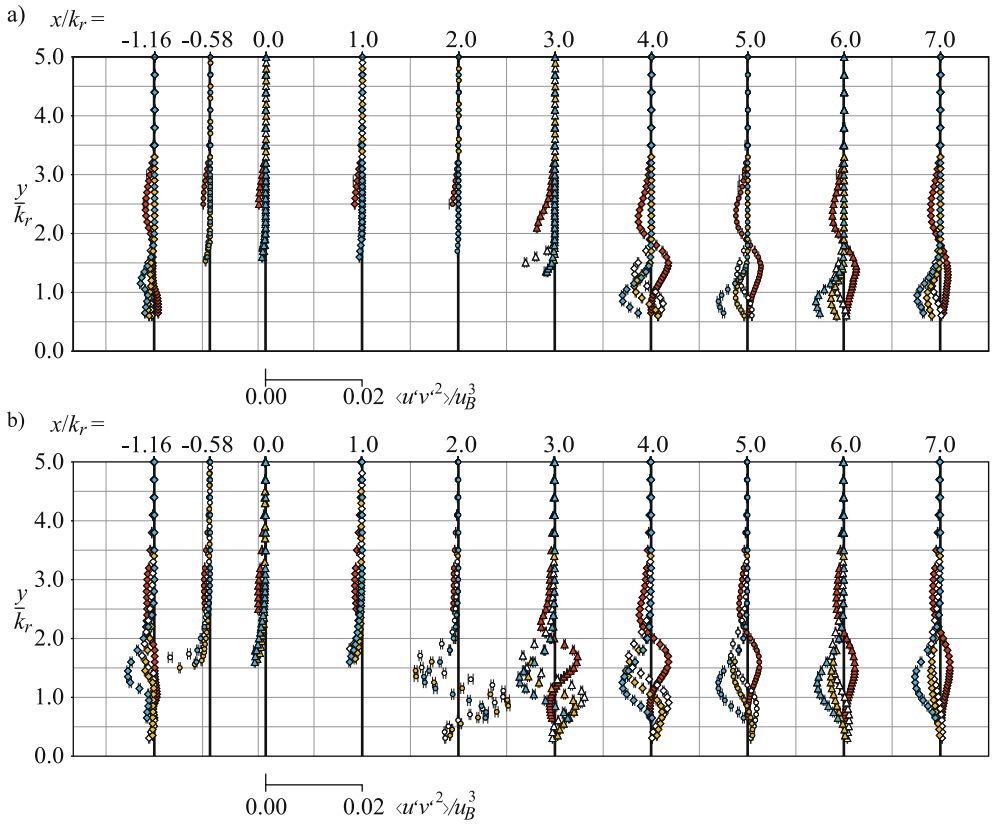

Fig. 18 Normalized triple correlation $\langle u'v'^2 \rangle / u_B^3$ at different axial positions for ♦ ● ▲ $c/k_r = 0.1$, ♦ ● ▲ $c/k_r = 0.3$, ◇ ○ △ $c/k_r = 0.5$, and ♦ ● ▲ $c/k_r = 1.0$ within the (**a**) $z/H = 0.0$-plane and (**b**) $z/H = 0.25$-plane

the variations of $\langle u'^3 \rangle$ were negligible within the entire gap. Similar to the Reynolds stresses, it can be assumed that the suppression of pronounced mean velocity gradients due to the low Reynolds number flow in the gap for $c/k_r = 0.1$ prevented the formation of turbulent structures as a result of the absence of lateral swirling motion. At the duct bottom, the negligibly small values of $\langle u'^3 \rangle$ indicated the absence of turbulent transport.

3.3.2 Triple velocity correlations in the inter-rib spacing

Separation of vortical flow structures with the shear layers at the rib trailing edges into the inter-rib spacing was reflected by an increase in the triple velocity correlations. Comparison of the distributions of $\langle u'^3 \rangle$ and $\langle u'v'^2 \rangle$ (Figs. 15, 16 and 18) with those of a detached transversely oriented square cylinder (Addai et al. 2022) allows for a distinction of wake configurations for $c/k_r = 0.1$ and $c/k_r \geq 0.3$. The $\langle u'^3 \rangle$ minima behind the rib trailing edges ($x/k_r = 1.0$ and 2.0) and the $\langle u'v'^2 \rangle$ double S-curves with two clear local minima and maxima in the near-wake ($x/k_r = 2.0$ and 3.0 in the $z/H = 0.25$-plane) were characteristic of the occurrence of two shear layers. In contrast to this, the absence of the $\langle u'^3 \rangle$ minimum behind the lower rib trailing edge and the $\langle u'v'^2 \rangle$ single S-curve with only one minimum and maximum indicated the predominance of one shear layer. The asymmetrically distributed minima and maxima were caused by flow close to the wall and its impact on downstream propagation of the flow structures separating at the rib trailing edge. For $c/k_r \geq 0.3$, decreasing maxima of the triple velocity correlations from $x/k_r \geq 4.0$ in the $z/H = 0.0$-plane and from $x/k_r \geq 3.0$ in the $z/H = 0.25$-plane indicated a decay of turbulent transport due to diffusion of the flow structures moving downstream. The peak values of $\langle u'^3 \rangle$ revealed flow regions with an intense transport of high-energy elongated turbulent flow structures with u'. Accordingly, local peak values of $\langle u'^3 \rangle$ were found at the height of the rib trailing edges in the immediate wake. The effect of the wall-bounded shear flow along the bottom duct wall on the wake disturbed the axial development of the lower free shear layer and led to a weaker development and faster decay of the lower peaks of the triple velocity correlation for decreasing c/k_r. The latter was not limited to the $\langle u'^3 \rangle$ distribution, but also occurred for the other triple velocity correlations, resulting in increasingly similar distributions for different c/k_r further downstream.

For $c/k_r = 0.1$, the distributions of $\langle u'^3 \rangle$ were antisymmetrical across (vertical) the shear layer, reached peak values on either side, and vanished at the outer ends of the shear

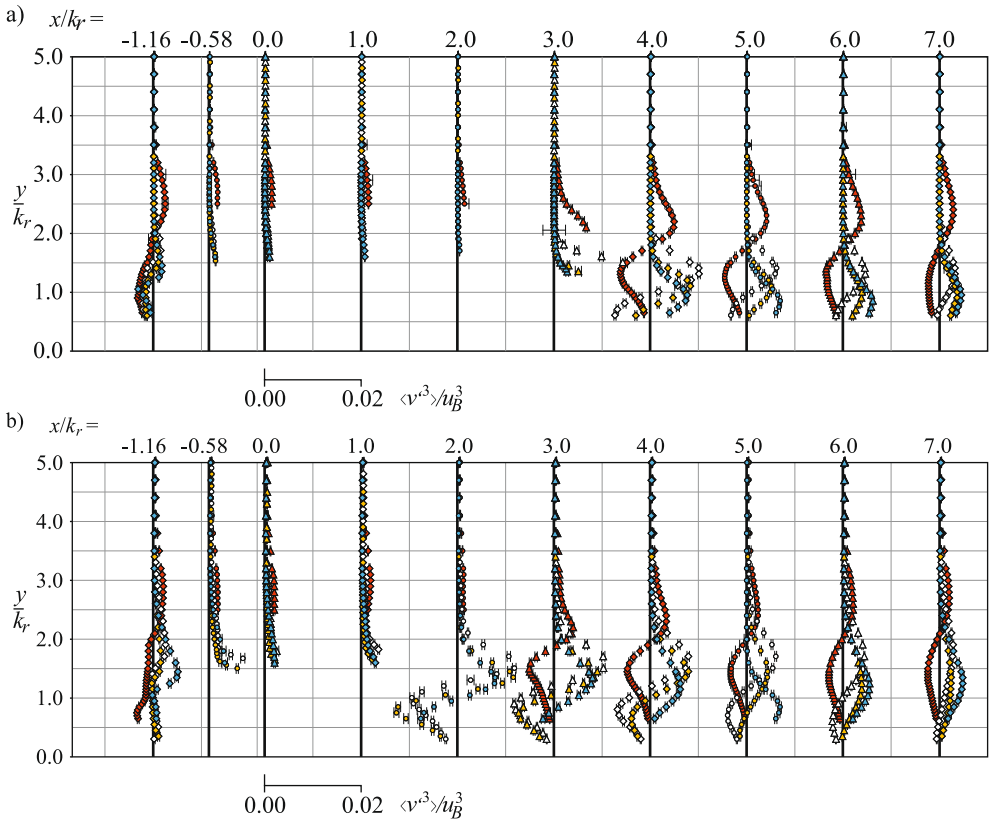

Fig. 19 Normalized triple correlation $\langle v'^3\rangle/u_B^3$ at different axial positions for ♦ ● ▲ $c/k_r = 0.1$, ♦ ● ▲ $c/k_r = 0.3$, ◊ ○ △ $c/k_r = 0.5$, and ♦ ● ▲ $c/k_r = 1.0$ in the (**a**) $z/H = 0.0$-plane and (**b**) $z/H = 0.25$-plane

layer. Their shapes resembled those of reattaching shear layers found in the wake of a wall-bound square cylinder (Agelinchaab and Tachie 2008) or a backward facing step (Chandrsuda and Bradshaw 1981). Maintenance of the comparatively high values of $\langle u'^3\rangle$ for $c/k_r = 0.1$ in the wake was attributed to the formation of a longitudinally stretched shear layer behind the upper rib trailing edge, providing a steady source for elongated vortical structure generation. $\langle u'^3\rangle$ and $\langle v'^3\rangle$ developed similarly (Figs. 15, 16, and 19) with opposite signs, indicating an unsteady flapping motion of flow structures that separated from the upper rib trailing edge with the shear layer (Mahmoodi-Jezeh and Wang 2020).

Turbulent transport of turbulence kinetic energy induced by the shedding of flow structures at the rib trailing edges persisted along the entire inter-rib spacing. This is obvious from the strongly varying triple velocity distributions of $\langle u'^2 v'\rangle$ and $\langle v'^3\rangle$ in vertical direction (Figs. 17 and 19). The vertical turbulent transport was highest behind the ribs and decreased with the decreasing gradients of $\langle u'^2 v'\rangle$ and $\langle v'^3\rangle$ further downstream. For $c/k_r \geq 0.3$, the double S-curve changed to a single S-curve due to the influence of the wall that caused the lower peak to vanish. Regions with high turbulent transport moved away from the wall with increasing c/k_r.

For $c/k_r = 0.1$, the turbulent transport away from and toward the wall was reduced slightly in axial direction due to the persistence of the stretched free shear layer and exceeded the corresponding values for $c/k_r \geq 0.3$. As can be seen from the comparison of the transport terms $T_k = -1/2\partial/\partial y\left[\langle u'^2 v'\rangle - \langle v'^3\rangle\right]$, the production terms $P_k = -\langle u'^2\rangle\,\partial\langle u\rangle/\partial x - \langle u'v'\rangle\,\partial\langle u\rangle/\partial y - \langle v'^2\rangle\,\partial\langle v\rangle/\partial y$, and the mean convection term $C_k = -1/2\langle v\rangle\,\partial/\partial y(\left[\langle u'^2\rangle + \langle v'^2\rangle\right]$ for the turbulence kinetic energy (here defined as $k_t = 1/2 \cdot \left[\langle u'^2\rangle + \langle v'^2\rangle\right]$ budget in the $z/H = 0.0$-plane shown in Fig. 20, turbulent transport contributed significantly to the turbulence kinetic energy in the inter-rib spacing. Although, the lack of the lateral flow component, the instantaneous spatial derivatives, and the pressure resulted in enormous simplifications of the turbulence budget equation for the highly three-dimensional flow field of divergent ribs, the distributions in Fig. 20 were assumed to be qualitatively representative due to the vanishing lateral mean velocity $\langle w\rangle$ in the symmetry plane ($z/H = 0.0$-plane). Nevertheless, even a small deviation from the condition $z/H = 0.0$ due to uncertainties in the orientation of the measurement volume would lead to considerable differences in the distributions shown in Fig. 20 and would invalidate the simplifications made with respect to symmetry.

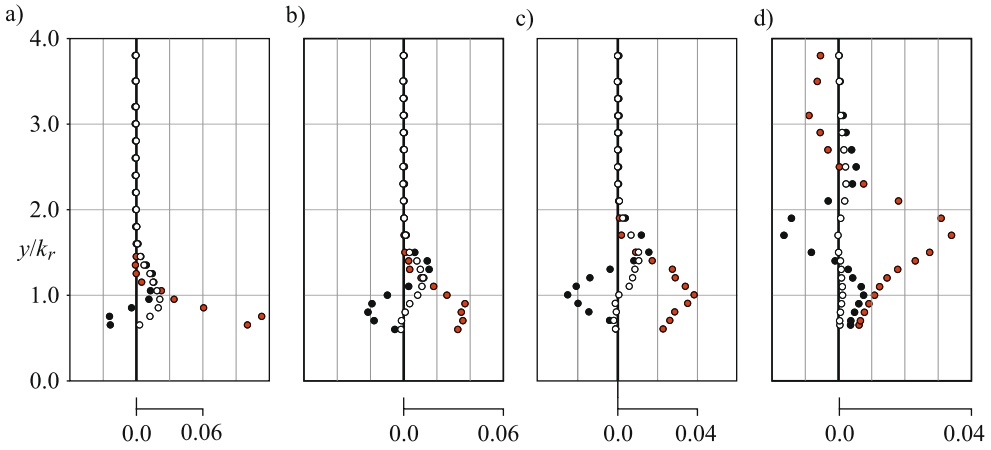

Fig. 20 Contribution from • production P_k, • turbulent transport T_k and ○ mean convection C_k to the turbulence kinetic energy budget for (**a**) $c/k_r = 0.1$, (**b**) $c/k_r = 0.3$, (**c**) $c/k_r = 0.5$, and (**d**) $c/k_r = 1.0$ at $x/k_r = 0.0$ in the $z/H = 0.0$-plane. Data normalized by mean bulk velocity and rib height

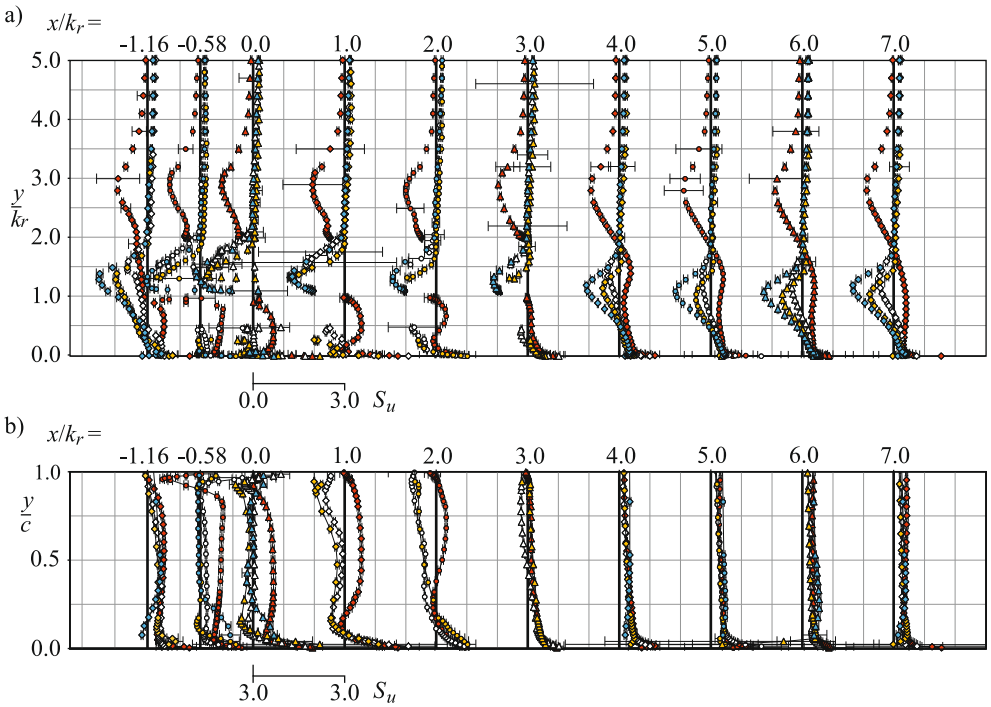

Fig. 21 Skewness $\langle u'^3\rangle/\langle u'^2\rangle^{3/2}$ at different axial positions (**a**) over the duct and (**b**) within the gap for ♦ • ▲ $c/k_r = 0.1$, ♦ • ▲ $c/k_r = 0.3$, ◊ ○ △ $c/k_r = 0.5$, and ♦ • ▲ $c/k_r = 1.0$ within the $z/H = 0.0$-plane

3.4 Skewness and kurtosis

The high-order statistics skewness $S_u = \langle u'^3\rangle/\langle u'^2\rangle^{3/2}$ and kurtosis $K_u = \langle u'^4\rangle/\langle u'^2\rangle^2$ are non-dimensional measures for the shape of the probability density function of a corresponding signal. Therefore, both provide temporal information about flow physics extracted from the probability density function shape: skewness describes the asymmetry and kurtosis determines the flatness. Their analyses were commonly applied to investigate turbulent flow structures in detail, e.g., for wall-bounded flows (Gad-el Hak and Bandyopadhyay 1994; Andreopoulos et al. 1984) as well as for separated flows (Simpson et al. 1981) or wakes (Mariotti and Buresti 2013; Ezadi Yazdi and ak Khoshnevis 2020). Skewness of $S_u = 0$ and excess kurtosis of $K_{u,e} = K_u - 3 = 0$ are characteristic for a Gaussian probability density function distributed symmetrically around the mean. Nonzero skewness values indicate the degree of temporal asymmetry of large-amplitude velocity fluctuations, while nonzero excess kurtosis values reveal information about the peakness of a

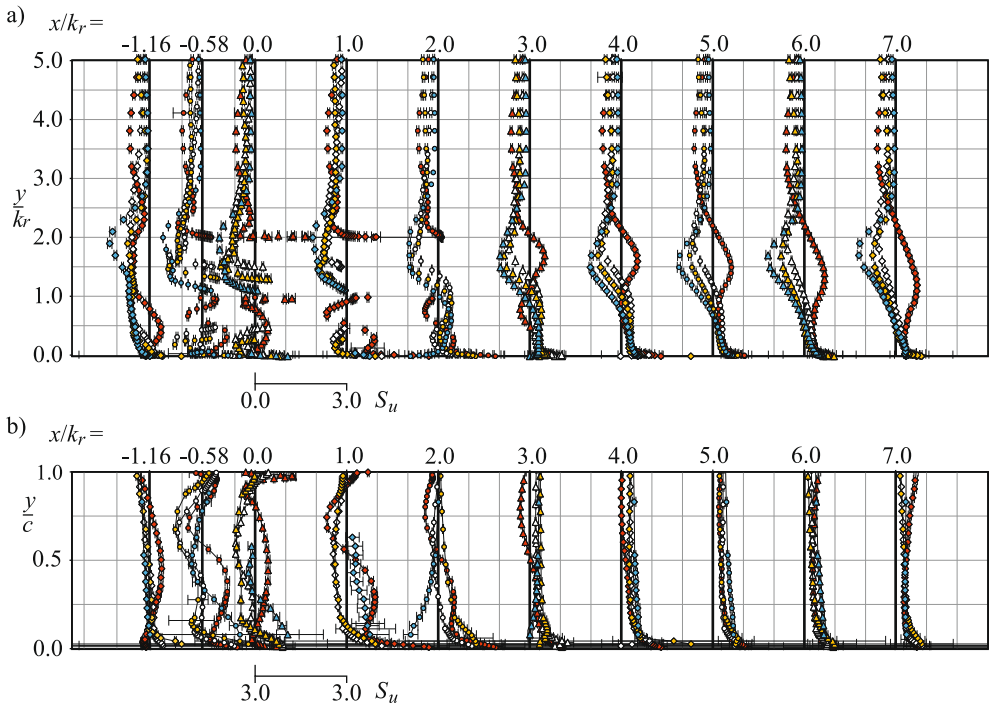

Fig. 22 Skewness $\langle u'^3\rangle/\langle u'^2\rangle^{3/2}$ at different axial positions (**a**) over the duct and (**b**) within the gap for ♦ • ▲ $c/k_r = 0.1$, ♦ • ▲ $c/k_r = 0.3$, ◊ ∘ △ $c/k_r = 0.5$, and ♦ • ▲ $c/k_r = 1.0$ within the $z/H = 0.25$-plane

temporal signal. The latter is associated with intermittent flow phenomena (Frisch 1995). Distributions of the skewness and excess kurtosis of the streamwise velocity fluctuations for the investigated flow configurations are presented in Figs. 21, 22, 23 and 24.

With the exception of $c/k_r = 0.3$ above the rib at $x/k_r = 0.0$, S_u and $K_{u,e}$ distributions were similar for $y/k_r \geq 4.0$ within the $z/H = 0.0$-plane. In the lateral direction ($z/H = 0.25$-plane), the distributions converged in the upper half of the duct and resembled each other for $y/k_r > 8.0$ (not shown). The dependency of high-order statistics on the varying flow configuration with c/k_r for $y/k_r < 4.0$ held also for the skewness and excess kurtosis. In general, the distributions for $c/k_r = 0.3$ and 0.5 differed only slightly with a small vertical offset, but deviated from $c/k_r = 0.1$ and $c/k_r = 1.0$.

3.4.1 Skewness and kurtosis close to the rib

Immediately above the upper rib tip in the duct symmetry plane, skewness reached negative peaks and excess kurtosis reached positive peaks for $c/k_r \leq 0.5$, while for $c/k_r = 1.0$, S_u and $K_{u,e}$ peaks were located $\Delta y/k_r \approx 1$ above the rib tip. Further downstream, high values of skewness and excess kurtosis occurred above the rib crest for all c/k_r in both measuring planes. S_u and $K_{u,e}$ peaks were reduced in the $z/H = 0.25$-plane compared to those in the $z/H = 0.0$-plane. According to previous studies about turbulent boundary layer flows (Simpson et al. 1981), the locations of negative S_u minima and positive $K_{u,e}$ maxima corresponded to the outer edge of the thin shear layer and can be attributed to large-amplitude negative (=low-speed compared to the mean) streamwise velocity fluctuations. They were the result of large vortical structures generated by the mean shear carrying fluid from the low-streamwise-velocity region within the shear layer outward. Since S_u and $K_{u,e}$ peaks coincided, the high excess kurtosis suggested an intermittent nature of these velocity fluctuations.

It was interesting to see that below the rib in the gap center ($x/k_r = -0.58$), skewness was increased only for $c/k_r = 1.0$. It was hypothesized that high speed flow structures shed at the lower rip tip moved into the gap center. For $c/k_r = 1.0$, the comparable low mean streamwise flow velocities (Figs. 5 and 6) in the gap caused the fluid carried by these flow structures to appear as large-amplitude positive (=high-speed compared to the mean) streamwise velocity fluctuations. On the contrary, for the $c/k_r \leq 0.5$, the flow acceleration in the gap caused high mean streamwise flow velocities without high streamwise velocity fluctuations.

3.4.2 Skewness and kurtosis in the inter-rib spacing

With the separation at the rib trailing edge, the wall-bounded shear layer transformed into a free shear layer. Similar skewness and excess kurtosis behavior as for the outer edge of the wall-bounded thin shear layer was found in the region above

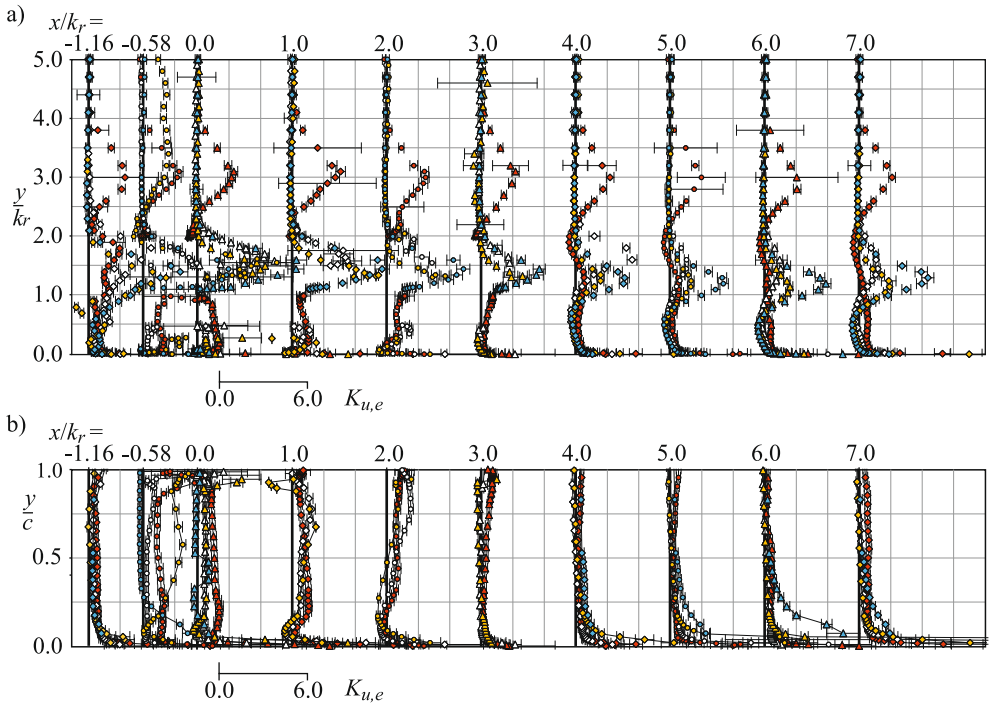

Fig. 23 Kurtosis $\langle u'^4\rangle/\langle u'^2\rangle^2$ at different axial positions (**a**) over the duct and (**b**) within the gap for ♦ ● ▲ $c/k_r = 0.1$, ♦ ● ▲ $c/k_r = 0.3$, ◊ ○ △ $c/k_r = 0.5$, and ♦ ● ▲ $c/k_r = 1.0$ within the $z/H = 0.0$-plane

the upper free shear layer in the wake within both measuring planes, with the exception of $c/k_r = 1.0$ in the $z/H = 0.25$-plane. Vortical structures originated from the shear layer transported fluid from the low-velocity wake region upward and increased the skewness and excess kurtosis. Highest values of S_u and $K_{u,e}$ occurred for a clearance-to-rib-height ratio of $c/k_r = 0.1$. In accordance with findings for turbulent wake flows (Mariotti and Buresti 2013; Ezadi Yazdi and ak Khoshnevis 2020), locations of the found negative skewness peaks were supposed to indicate the outer edge of the free shear layers. For $c/k_r = 1.0$, skewness and excess kurtosis indicated further upward motion of vortical structures which were generated in the upper shear layer. The resulting vertical location offset of $\Delta y/k_r = 1.0$ for S_u and $K_{u,e}$ peaks for $c/k_r = 1.0$ was attributed to the wider vertical spreading of the upper shear layer for $c/k_r = 1.0$ than for $c/k_r \leq 0.5$. The consistency of S_u and $K_{u,e}$ peaks over the complete rib-pitch section highlighted the dominance of large-amplitude negative streamwise velocity fluctuations in this region. In the near wake region ($0.0 \leq x/k_r \leq 3.0$), a downward transport of fluid from the low-velocity wake region with turbulent structures was supposed to cause negative skewness peaks and positive excess kurtosis below the lower free shear layer for $c/k_r \geq 0.3$. They decayed further downstream with the diffusion of the lower shear layer.

Starting from the outer edge of the upper free shear layer, skewness increased with increasing proximity to the wall and changed its sign from negative to positive in the wake. The sign change of the skewness (Figs. 21 and 22) occurred close to the region where Reynolds shear stress $-\langle u'v'\rangle$ (Fig. 11 a and b) reached its maxima for all c/k_r. Further zero-crossings of the skewness for $c/k_r = 1.0$ at $x/k_r = 3.0$ and 4.0 in the $z/H = 0.25$-plane corresponded to the Reynolds shear stress minimum. The reduced skewness resulted from an intense momentum exchange in this region without a prevailing temporal dominance of high-speed or low-speed streamwise velocity fluctuations. The slightly flat-top shaped probability density function indicated by an excess kurtosis of $K_{u,e} < 0$ in this region was a further consequence of the intense mixing suppressing large-amplitude velocity fluctuations or intermittent flow nature. Interestingly, positive skewness peaks occurred in the wake at $x/k_r \geq 3.0$ for $c/k_r = 1.0$. Following the analysis of cylinder wake flows (Fabris 1983), the positive skewness peaks resulted from the movement of turbulent structures which entrained high-speed fluid by their rotational motion at the shear layer edges and carried it toward the wake.

Similar to the near-wall region of turbulent boundary layers (Andreopoulos et al. 1984; Gad-el Hak and Bandyopadhyay 1994), high values of skewness and excess kurtosis occurred very close to the duct bottom wall at all axial positions for all clearance-to-rib-height ratios with exception of the recirculation region for $c/k_r = 0.1$ where negative skewness was expected (Simpson et al. 1981). The increase of positive skewness accompanied by the tremendous peak in the positive excess kurtosis very close to the duct

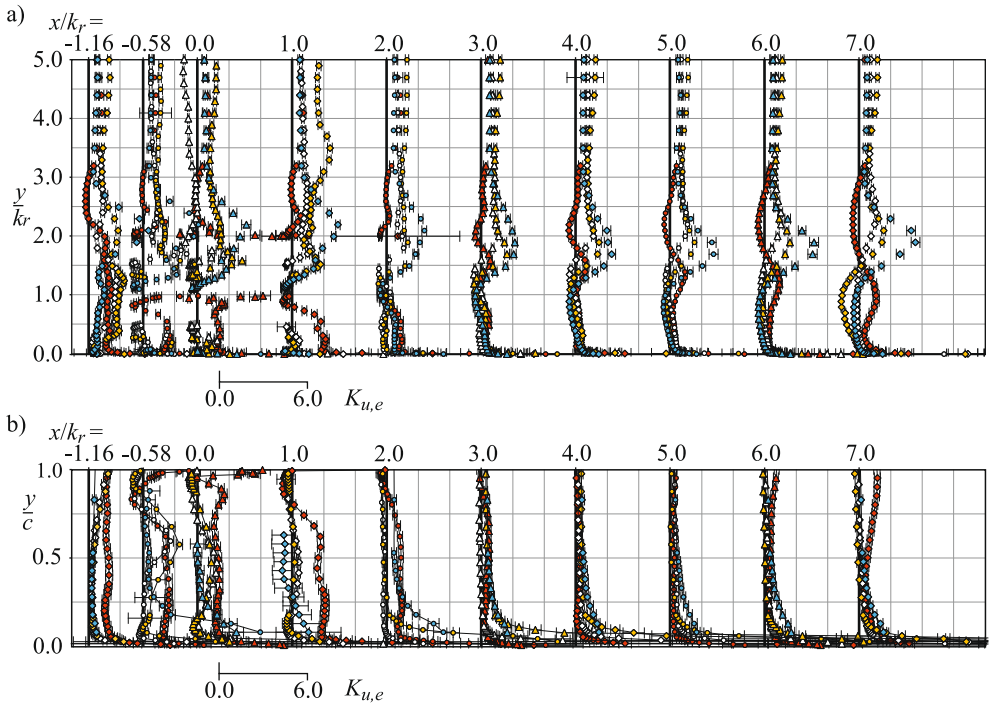

Fig. 24 Kurtosis $\langle u'^4\rangle/\langle u'^2\rangle^2$ at different axial positions (**a**) over the duct and (**b**) within the gap for ♦ ● ▲ $c/k_r = 0.1$, ♦ ● ▲ $c/k_r = 0.3$, ◊ ○ △ $c/k_r = 0.5$, and ♦ ● ▲ $c/k_r = 1.0$ within the $z/H = 0.25$-plane

bottom wall indicated the dominance of large-amplitude positive streamwise velocity fluctuations. S_u and $K_{u,e}$ increases were attributed to the pushing-in of high-velocity fluid from the region above the viscous dominated near wall region, resulting in a more frequently occurrence of large positive streamwise velocity fluctuations than of large negative streamwise fluctuations.

4 Conclusion

The turbulent flow field in a square duct with detached 60° divergent ribs applied to one wall was investigated for different clearance-to-rib-height ratios in the range of 0.1–1.0. LDA measurements were performed to yield deep insights into the turbulent flow field. It was shown that for detached divergent ribs, a geometry-induced secondary fluid motion occurred above and below the rib with flow velocities depending on the clearance-to-rib-height ratio. The development of shear layers separating at the rib trailing edges further downstream was strongly affected by the formation of the secondary flow field. For varying clearance-to-rib-height ratios different flow configurations in the inter-rib spacing were obtained. In the duct's symmetry plane, the shear layers separated at the rib trailing edges. They developed parallel to the bottom duct wall further downstream. In lateral direction, the upper shear layer pivoted upward due to the decreasing downward fluid motion. The formation of a large recirculation region between the leeward rib surface and the duct bottom wall due to the reattachment of the shear layer from the upper rib trailing edge in the case of attached ribs was prevented by the fluid exiting the gap below the detached divergent ribs. Nevertheless, a recirculation region was found for the smallest clearance-to-rib-height ratio. For $c/k_r = 0.1$, the flow exiting the gap was too weak to flow against the adverse pressure gradient and the wall-bounded flow in the rib rear detached with an upward motion of the lower free shear layer. A thin recirculation region developed and ended further downstream with the reattachment of the upper free shear layer. For $c/k_r \geq 0.3$, the high flow velocities at the gap outlet enabled the fluid to overcome the adverse pressure gradient without a detachment of the wall-bounded flow and a permanent reattachment of the separated shear layers, while secondary flow motion persisted. With decreasing wall proximity, the effect of the wall on the flow field in the inter-rib spacing reduced. The vertical propagation of shear layers increased with increasing clearance-to-rib-height ratios. For $c/k_r = 1.0$, the lower mean vertical flow velocities above the ribs attenuated an intense interaction of the separated free shear layers with the wall-bounded flow, resulting in a less disturbed development of both shear layers further downstream.

Turbulent structures originated from the shear layers. Peaks of Reynolds stresses and triple velocity correlations coincided with the three-dimensional development of the shear layers. The differences found in the mean flow fields

for varying c/k_r were reflected by the Reynolds stress and triple velocity correlation distributions. Increases of the axial Reynolds normal stress $\langle u'^2 \rangle$ and the triple velocity correlation $\langle u'^3 \rangle$ in lateral direction in the shear layers along the rib top and bottom surfaces were attributed to a secondary flow-induced lateral transport of turbulent flow structures generated near the duct symmetry plane and deflected toward the side walls. Within the inter-rib spacing, Reynolds stresses and triple velocity correlation reached peak values in the upper shear layer. In general, both Reynolds normal stresses were of comparable order of magnitude, but far away from unity in the rib wake. The variation of the negative mean flow velocity $\langle v \rangle$ caused the free shear layers to develop downstream with different vertical extent as indicated by the skewness distributions, which caused variations in the Reynolds stresses and triple velocity correlations. Kurtosis suggested intermittent flow at the outer edges of the free shear layers where vortical motion of turbulent structures carried fluid from the low-velocity regions of the shear layer outward. Separated flow structures underwent a flapping motion while moving downstream as indicated by the triple velocity correlations. Maximum $-\langle u'v' \rangle$ and $\langle u'^2 \rangle$ occurred in a region below the outer edge of the upper shear layer, where velocity fluctuations occurred without large amplitudes and predominate velocity due to the high flow mixing. For decreasing c/k_r, Reynolds stress peak regions and regions of turbulent transport indicated by triple velocity correlation distributions shifted toward the bottom duct wall. The local Reynolds stress maxima and triple velocity correlation maxima/minima were located nearest to the bottom duct wall in the $z/H = 0.0$-plane. With an increase of $\langle v \rangle$ in lateral direction, the upper free shear layer was less deflected toward the bottom duct wall. The increase in Reynolds stresses near the duct side walls was attributed to laterally deflected turbulent structured by the secondary flow field. For $c/k_r = 1.0$, the distributions indicated a reduced propagation of the free shear layers and turbulent flow structures toward the bottom duct wall due to the reduced negative mean vertical velocity from the secondary flow field above the rib and the increased mean vertical velocity of the fluid exiting the gap below the rib.

Acknowledgements The authors would like to thank the Deutsche Forschungsgemeinschaft (DFG) for funding the work within the DFG project RU 2264/2-1.

Author Contributions SR wrote the manuscript text and prepared all figures. All authors reviewed the manuscript. All authors have read and agreed to the published version of the manuscript.

Funding Open Access funding enabled and organized by Projekt DEAL. This study was funded by DFG project RU 2264/2-1.

Data availability The prepared data can be obtained for validation studies from the corresponding author and from the KITopen repository at https://doi.org/10.35097/1s45thff1jfwfsen.

Declarations

Conflict of interest The authors declare that they have no conflict of interest.

References

Addai S, Fang X, Mante AA et al (2022) The wake dynamics behind a near-wall square cylinder. J Fluids Eng 144(5):051305. https://doi.org/10.1115/1.4052675

Agelinchaab M, Tachie MF (2008) PIV study of separated and reattached open channel flow over surface mounted blocks. J Fluids Eng 130(6):061206. https://doi.org/10.1115/1.2911677

Ahn J, Lee JS (2010) Large eddy simulation of flow and heat transfer in a channel with a detached rib array. Int J Heat Mass Transf 53(1):445–452. https://doi.org/10.1016/j.ijheatmasstransfer.2009.09.012

Ahn J, Choi H, Lee JS (2005) Large eddy simulation of flow and heat transfer in a channel roughened by square or semicircle ribs. J Turbomach 172(2):263–269. https://doi.org/10.1115/1.1811098

Andreopoulos J, Bradshaw P (1981) Measurements of turbulence structure in the boundary layer on a rough surface. Bound-Layer Meteorol 20:201–213. https://doi.org/10.1007/BF00119902

Andreopoulos J, Durst F, Zaric Z et al (1984) Influence of Reynolds number on characteristics of turbulent wall boundary layers. Exp Fluids 2:7–16. https://doi.org/10.1007/BF00266313

Bailey SCC, Martinuzzi RJ, Kopp GA (2002) The effects of wall proximity on vortex shedding from a square cylinder: three-dimensional effects. Phys Fluids 14(12):4160–4177. https://doi.org/10.1063/1.1514972

Benedict L, Gould R (1996) Towards better uncertainty estimates for turbulence statistics. Exp Fluids 22:129–136. https://doi.org/10.1007/s003480050030

Bhushan B, Singh R (2010) A review on methodology of artificial roughness used in duct of solar air heaters. Energy 35(1):202–212. https://doi.org/10.1016/j.energy.2009.09.010

Bosch G, Kappler M, Rodi W (1996) Experiments on the flow past a square cylinder placed near a wall. Exp Therm Fluid Sci 13(3):292–305. https://doi.org/10.1016/S0894-1777(96)00087-8

Buchhave P, George WK, Lumley JL (1979) The measurement of turbulence with the laser-doppler anemometer. Annu Rev Fluid Mech 11(1):443–503. https://doi.org/10.1146/annurev.fl.11.010179.002303

Cardwell ND, Vlachos PP, Thole KA (2011) Developing and fully developed turbulent flow in ribbed channels. Exp Fluids 50:1357–1371. https://doi.org/10.1007/s00348-010-0993-y

Chandrsuda C, Bradshaw P (1981) Turbulence structure of a reattaching mixing layer. J Fluid Mech 110:171–194. https://doi.org/10.1017/S0022112081000670

Coletti F, Cresci I, Arts T (2013) Spatio-temporal analysis of the turbulent flow in a ribbed channel. Int J Heat Fluid Flow 44:181–196. https://doi.org/10.1016/j.ijheatfluidflow.2013.05.020

Durão DFG, Gouveia PST, Pereira JCF (1991) Velocity characteristics of the flow around a square cross section cylinder placed near a channel wall. Exp Fluids 11:341–350. https://doi.org/10.1007/BF00211788

Endrikat S, Newton R, Modesti D et al (2022) Reorganisation of turbulence by large and spanwise-varying riblets. J Fluid Mech 952:A27. https://doi.org/10.1017/jfm.2022.897

Ezadi Yazdi J, Khoshnevis AB (2020) Comparing the wake behind circular and elliptical cylinders in a uniform current. SN Appl Sci 2:2523–3971. https://doi.org/10.1007/s42452-020-2698-z

Fabris G (1983) Higher-order statistics of turbulent fluctuations in the plane wake. Phys Fluids 26(6):1437–1445. https://doi.org/10.1063/1.864313

Fang X, Yang Z, Wang BC et al (2015) Highly-disturbed turbulent flow in a square channel with v-shaped ribs on one wall. Int J Heat Fluid Flow 56:182–197. https://doi.org/10.1016/j.ijheatfluidflow.2015.07.008

Fang X, Yang Z, Wang BC et al (2017) Large-eddy simulation of turbulent flow and structures in a square duct roughened with perpendicular and v-shaped ribs. Phys Fluids 29(6):065110. https://doi.org/10.1063/1.4985715

Frisch U (1995) Turbulence: the legacy of A. N. Kolmogorov. Cambridge University Press, London. https://doi.org/10.1017/CBO9781139170666

Gad-el Hak M, Bandyopadhyay PR (1994) Reynolds number effects in wall-bounded turbulent flows. Appl Mech Rev 47(8):307–365. https://doi.org/10.1115/1.3111083

Gao X, Sundén B (2004) Effects of inclination angle of ribs on the flow behavior in rectangular ducts. J Fluids Eng 126(4):692–699. https://doi.org/10.1115/1.1778715

Gao X, Sundén B (2004) PIV measurement of the flow field in rectangular ducts with 60° parallel, crossed and V-shaped ribs. Exp Therm Fluid Sci 28(6):639–653. https://doi.org/10.1016/j.expthermflusci.2003.10.005

García-Mayoral R, Jiménez J (2011) Drag reduction by riblets. Philos Trans R Soc A 369(1940):1412–1427. https://doi.org/10.1098/rsta.2010.0359

George WK (1988) Quantitative measurement with the burst-mode laser doppler anemometer. Exp Therm Fluid Sci 1(1):29–40. https://doi.org/10.1016/0894-1777(88)90045-3

Graham A, Sewall E, Thole KA (2004) Flowfield measurements in a ribbed channel relevant to internal turbine blade cooling. Turbo Expo: Power for Land, Sea, and Air 3:383–391. https://doi.org/10.1115/GT2004-53361

Han JC (1984) Heat transfer and friction in channels with two opposite rib-roughened walls. J Heat Transf 106(4):774–781. https://doi.org/10.1115/1.3246751

Han JC (2004) Recent studies in turbine blade cooling. Int J Rotating Mach 10(6):443–457. https://doi.org/10.1155/S1023621X04000442

He C, Liu Y, Peng D et al (2016) Measurement of flow structures and heat transfer behind a wall-proximity square rib using TSP. PIV and split-fiber film. Exp Fluids 57(165):1–18. https://doi.org/10.1007/s00348-016-2262-1

Hirota M, Yokosawa H, Fujita H (1992) Turbulence kinetic energy in turbulent flows through square ducts with rib-roughened walls. Int J Heat Fluid Flow 13(1):22–29. https://doi.org/10.1016/0142-727X(92)90056-F

Jia R, Sundén B, Fahri M (2005) Computational analysis of heat transfer enhancement in square ducts with V-shaped ribs: turbine blade cooling. J Heat Transf 127:425–433. https://doi.org/10.1115/1.1865220

Kumahor S, Tachie MF (2022) Turbulent flow around rectangular cylinders with different streamwise aspect ratios. J Fluids Eng 144(5):051304. https://doi.org/10.1115/1.4052633

Liou TM, Hwang JJ, Chen SH (1992) Turbulent transport phenomena in a channel with periodic rib turbulators. J Thermophys Heat Transf 6:513–521. https://doi.org/10.2514/3.390

Liou TM, Wang WB, Chang YJ (1995) Holographic interferometry study of spatially periodic heat transfer in a channel with ribs detached from one wall. J Heat Transf 117(1):32–39. https://doi.org/10.1115/1.2822319

Liou TM, Yang CP, Lee HL (1997) LDV measurements of spatially periodic flows over a detached solid-rib array. J Fluids Eng 119(2):383–389. https://doi.org/10.1115/1.2819145

Lohász MM, Rambaud P, Benocci C (2006) Flow features in a fully developed ribbed duct flow as a result of MILES. Flow Turbul Combust 63:59–76. https://doi.org/10.1007/s10494-006-9037-3

Mahmoodi-Jezeh SV, Wang BC (2020) Direct numerical simulation of turbulent flow through a ribbed square duct. J Fluid Mech 900:A18. https://doi.org/10.1017/jfm.2020.452

Mahmoodi-Jezeh S, Wang BC (2022) Direct numerical simulation of turbulent duct flow with inclined or V-shaped ribs mounted on one wall. J Fluid Mech 932:A48. https://doi.org/10.1017/jfm.2021.1028

Mariotti A, Buresti G (2013) Experimental investigation on the influence of boundary layer thickness on the base pressure and near-wake flow features of an axisymmetric blunt-based body. Exp Fluids 54:1432–1114. https://doi.org/10.1007/s00348-013-1612-5

Martinuzzi RJ, Bailey SCC, Kopp GA (2003) Influence of wall proximity on vortex shedding from a square cylinder. Exp Fluids 34:585–596. https://doi.org/10.1007/s00348-003-0594-0

Marumo E, Suzuki K, Sato T (1985) Turbulent heat transfer in a flat plate boundary layer disturbed by a cylinder. Int J Heat Fluid Flow 6(4):241–248. https://doi.org/10.1016/0142-727X(85)90056-6

Nakagawa S, Nitta K, Senda M (1999a) An experimental study on unsteady turbulent near wake of a rectangular cylinder in channel flow. Exp Fluids 28:284–294. https://doi.org/10.1007/s003480050353

Nakagawa S, Senda M, Hiraide A et al (1999b) Heat transfer characteristics in a channel flow with a rectangular cylinder. JSME Int J Ser B 42(2):188–196. https://doi.org/10.1299/jsmeb.42.188

Nakagawa S, Senda M, Kikkawa S et al (1998) Heat transfer in channel flow around a rectangular cylinder. Heat Transf Jpn Res 27(1):84–97 https://doi.org/10.1002/(SICI)1520-6556(1998)27:1<84::AID-HTJ7>3.0.CO;2-T

Olsson CO, Sundén B (1998) Experimental study of flow and heat transfer in rib-roughened rectangular channels. Exp Therm Fluid Sci 16(4):349–365. https://doi.org/10.1016/S0894-1777(97)10034-6

Panigrahi PK (2009) PIV investigation of flow behind surface mounted detached square cylinder. J Fluids Eng 131(1):011202. https://doi.org/10.1115/1.3026721

Park Y, Cho Y, Lee C (2001). Vortex shedding around a square cylinder near a wall. https://doi.org/10.2514/6.2001-450

Petukhov BS (1970) Heat transfer and friction in turbulent pipe flow with variable physical properties. Adv Heat Transf 6:503–564. https://doi.org/10.1016/S0065-2717(08)70153-9

Pirozzoli S, Modesti D, Orlandi P et al (2018) Turbulence and secondary motions in square duct flow. J Fluid Mech 840:631–655. https://doi.org/10.1017/jfm.2018.66

Rau G, Cakan M, Moeller D, Arts T (1998) The effect of periodic ribs on the local aerodynamic and heat transfer performance of a straight cooling channel. J Turbomach Trans ASME 120:368–375. https://doi.org/10.1115/1.2841415

Ruck S, Arbeiter F (2018) Detached eddy simulation of turbulent flow and heat transfer in cooling channels roughened by variously

shaped ribs on one wall. Int J Heat Mass Transf 118:388–401. https://doi.org/10.1016/j.ijheatmasstransfer.2017.10.094
Ruck S, Arbeiter F (2021) LDA measurements in a one-sided ribbed square channel at Reynolds numbers of 50,000 and 100,000. Exp Fluids 62:232. https://doi.org/10.1007/s00348-021-03313-5
Ruck S, Arbeiter F (2022) Measurements of turbulent transport in a square channel with one ribbed wall. J Fluids Eng 144(7):071304. https://doi.org/10.1115/1.4053442
Ruck S, Arbeiter F, Brenneis B et al (2019) Thermal-hydraulic study on rib and dimple structures for cooling the First Wall of DEMO. Fusion Eng Des 146:2144–2148. https://doi.org/10.1016/j.fusengdes.2019.03.125
Satta F, Simoni D, Tanda G (2012) Experimental investigation of flow and heat transfer in a rectangular channel with 45° angled ribs on one/two walls. Exp Therm Fluid Sci 37:46–56. https://doi.org/10.1016/j.expthermflusci.2011.09.020
Sewall EA, Tafti DK (2004) Large eddy simulation of the developing region of a stationary ribbed internal turbine blade cooling channel. Power for Land, Sea, and Air, Turbo Expo. https://doi.org/10.1115/GT2004-53832
Shi LL, Liu YZ, Wan JJ (2010a) Influence of wall proximity on characteristics of wake behind a square cylinder: PIV measurements and POD analysis. Exp Therm Fluid Sci 34(1):28–36. https://doi.org/10.1016/j.expthermflusci.2009.08.008
Shi LL, Liu YZ, Sung HJ (2010b) On the wake with and without vortex shedding suppression behind a two-dimensional square cylinder in proximity to a plane wall. J Wind Eng Ind Aerodyn 98(10):492–503. https://doi.org/10.1016/j.jweia.2010.03.002
Simpson RL, Chew YT, Shivaprasad BG (1981) The structure of a separating turbulent boundary layer. Part 2. Higher-order turbulence results. J Fluid Mech 113:53–73. https://doi.org/10.1017/S0022112081003406
Sreekesh K, Tafti DK, Vengadesan S (2021) Large-eddy simulation investigation of modified rib shapes on heat transfer in a ribbed duct. J Heat Transf. doi 10(1115/1):4051507
Tachie MF, Shah MK (2008) Favorable pressure gradient turbulent flow over straight and inclined ribs on both channel walls. Phys Fluids 20(9):095103. https://doi.org/10.1063/1.2973205
Tanda G (2011) Effect of rib spacing on heat transfer and friction in a rectangular channel with 45° angled rib turbulators on one/two walls. Int J Heat Mass Transf 54(5):1081–1090. https://doi.org/10.1016/j.ijheatmasstransfer.2010.11.015
Tennekes H, Lumley JL (1972) A first course in turbulence. MIT Press, Cambridge
Topas GmbH (2019) Atomizer Aerosol Generator ATM 210 product sheet. Topas GmbH, Dresden
VDI (2010) VDI heat atlas, 2nd edn. Springer, Berlin
Wang L, Sundén B (2007) Experimental investigation of local heat transfer in a square duct with various-shaped ribs. Heat Mass Transf 43(759):759–766. https://doi.org/10.1007/s00231-006-0190-y
Wang XK, Tan SK (2008) Comparison of flow patterns in the near wake of a circular cylinder and a square cylinder placed near a plane wall. Ocean Eng 35(5):458–472. https://doi.org/10.1016/j.oceaneng.2008.01.005
Wang L, Salewski M, Sundén B (2010) Turbulent flow in a ribbed channel: flow structures in the vicinity of a rib. Exp Therm Fluid Sci 34:165–176. https://doi.org/10.1016/j.expthermflusci.2009.10.005
Yao M, Nakatani M, Suzuki K (1989) Flow visualization and heat transfer experiments in a duct with a staggered array of cylinders. Exp Therm Fluid Sci 2(2):193–200. https://doi.org/10.1016/0894-1777(89)90033-2